An environmental dependence of the physical and structural properties in the Hydra Cluster galaxies

Ciria Lima-Dias[1]⋆, Antonela Monachesi[1,2], Sergio Torres-Flores[1], Arianna Cortesi[3,4], Daniel Hernández-Lang[5], Carlos Eduardo Barbosa[3,6], Claudia Mendes de Oliveira[3], Daniela Olave-Rojas[7], Diego Pallero[1], Laura Sampedro[3], Alberto Molino[3], Fabio R. Herpich[3], Yara L. Jaffé[8], Ricardo Amorín[1,2], Ana L. Chies-Santos[9], Paola Dimauro[10], Eduardo Telles[10], Paulo A. A. Lopes[4], Alvaro Alvarez-Candal[10,11], Fabricio Ferrari[12], Antonio Kanaan[13], Tiago Ribeiro[14], William Schoenell[15]

[1] *Departamento de Astronomía, Universidad de La Serena, Av. Cisternas 1200, La Serena, Chile*
[2] *Instituto de Investigación Multidisciplinar en Ciencia y Tecnología, Universidad de La Serena, Raúl Bitrán 1305, La Serena, Chile*
[3] *Instituto de Astronomia, Geofísica e Ciências Atmosféricas da Universidade de São Paulo, Cidade Universitária, CEP:05508-900, São Paulo, SP, Brazil*
[4] *Observatório do Valongo, Universidade Federal do Rio de Janeiro, Ladeira Pedro Antônio 43, Rio de Janeiro, RJ, 20080-090, Brazil*
[5] *Faculty of Physics, Ludwig-Maximilians-Universität, Scheinerstr. 1, 81679 Munich, Germany*
[6] *Steward Observatory, University of Arizona, 933 N Cherry Ave, Tucson, AZ 85719, USA*
[7] *Departamento de Tecnologías Industriales, Universidad de Talca, Los Niches km 1, Curicó, Chile*
[8] *Instituto de Física y Astronomía, Universidad de Valparaíso, Avda. Gran Bretaña 1111 Valparaíso, Chile*
[9] *Departamento de Astronomia, Instituto de Física, Universidade Federal do Rio Grande do Sul (UFRGS), Av. Bento Gonçalves 9500, Porto Alegre, RS, Brazil*
[10] *Observatório Nacional / MCTIC, Rua General José Cristino 77, Rio de Janeiro, RJ, 20921-400, Brazil*
[11] *Instituto Universitario de Física Aplicada a las Ciencias y las Tecnologías, Universidad de Alicante, San Vicent del Raspeig, E03080, Alicante, Spain*
[12] *Instituto de Matemática Estatística e Física, Universidade Federal do Rio Grande, Rio Grande, RS, 96201-900, Brazil*
[13] *Departamento de Física, Centro de Ciencias Físicas e Matemáticas, Universidade Federal de Santa Catarina, Florianópolis, SC, 88040-900, Brazil*
[14] *LSST Project Office, 950 N. Cherry Ave., Tucson, AZ 85719, USA*
[15] *GMTO Corporation 465 N. Halstead Street, Suite 250 Pasadena, CA 91107*

ABSTRACT

The nearby Hydra Cluster ($\sim$50 Mpc) is an ideal laboratory to understand, in detail, the influence of the environment on the morphology and quenching of galaxies in dense environments. We study the Hydra cluster galaxies in the inner regions ($1R_{200}$) of the cluster using data from the Southern Photometric Local Universe Survey (S-PLUS), which uses 12 narrow and broad band filters in the visible region of the spectrum. We analyse structural (Sérsic index, effective radius) and physical (colours, stellar masses and star formation rates) properties. Based on this analysis, we find that $\sim$88 percent of the Hydra cluster galaxies are quenched. Using the Dressler-Schectman test approach, we also find that the cluster shows possible substructures. Our analysis of the phase-space diagram together with `DBSCAN` algorithm indicates that Hydra shows an additional substructure that appears to be in front of the cluster centre, which is still falling into it. Our results, thus, suggest that the Hydra Cluster might not be relaxed. We analyse the median Sérsic index as a function of wavelength and find that for red (($u-r$) $\geq$2.3) and early-type galaxies it displays a slight increase towards redder filters (13 and 18 percent, for red and early-type respectively) whereas for blue+green (($u-r$)<2.3) galaxies it remains constant. Late-type galaxies show a small decrease of the median Sérsic index toward redder filters. Also, the Sérsic index of galaxies, and thus their structural properties, do not significantly vary as a function of clustercentric distance and density within the cluster; and this is the case regardless of the filter.

Key words: galaxies: clusters: general – galaxies: fundamental parameters – galaxies: structure

1 INTRODUCTION

One of the many remarkable and still open questions in extragalactic astronomy is: How do galaxies evolve with/within environment? Several studies have addressed this issue, generally based on pioneer works, which determined a relation between the environment in which galaxies reside and their physical properties (Oemler 1974; Davis & Geller 1976; Butcher & Oemler 1978; Dressler 1980; Postman & Geller 1984). In particular Dressler (1980) detected an increase in the fraction of elliptical and S0 galaxies (early-type galaxies, or ETGs) as a function of increasing the environmental density, while the opposite is observed for spiral galaxies (late-type galaxies, or LTGs) (Gunn & Gott 1972; Whitmore & Gilmore 1991; Poggianti et al. 2001; Boselli et al. 2005; Fasano et al. 2015). This indicates that the environment is playing a crucial role on the morphology and stellar production of galaxies and is one of the main mechanisms often associated to the star-formation (SF) quenching on the Local Universe. In addition, internal process such as mass quenching, which is driven by gas outflows produced by stellar winds and supernovae feedback (Larson 1974; Dekel & Silk 1986; Efstathiou 2000; Cantalupo 2010; Peng et al. 2010b) or due to active galactic nuclei (AGN) activity (Croton et al. 2006; Fabian 2012; Cicone et al. 2014)) also has its influence. In the case of AGN activity, will be specially relevant for massive galaxies ($M_\star 10^{10} M_\odot$) (Peng et al. 2010b; Cora et al. 2019).

Environmental effects are drastically enhanced in clusters due to the tremendous gravitational potential. Fast and aggressive encounters between satellite galaxies become recurring. This process, known as harassment, is capable to destroy the disks of the satellites affected, becoming specially relevant in the inner parts of clusters (Moore et al. 1998, 1999; Duc & Bournaud 2008; Smith et al. 2015). On the other hand, interaction between the galaxy and the intracluster medium can strip the gas component of galaxies. This phenomena is called ram-pressure or strangulation (Gunn & Gott 1972; Abadi et al. 1999; Quilis et al. 2000; Balogh & Morris 2000; Vollmer et al. 2001; Jaffé et al. 2015; Peng et al. 2015), depending the strength of the stripping. Within a cluster, the galaxies inhabiting the core are usually the most massive ones, and most of them being quenched at early times. LTGs within clusters, are often found among the satellites at the outskirts (Dressler et al. 1997; Fasano et al. 2000; Postman et al. 2005; Desai et al. 2007). In general LTGs are the less massive components and are strongly susceptible to the influence of the processes aforementioned.

More recently using data from the Sloan Digital Sky Survey (SDSS; Abazajian et al. 2009), Liu et al. (2019) compared the fractions of ETGs and LTGs, and the fraction of main sequence galaxies (MSG) and quenched galaxies (QG) relative to different environments (voids, sheets, filaments, and clusters), finding that the star-forming properties of galaxies changed more dramatically than their structural properties. This means that a galaxy will stop forming stars before any morphological change can take place. They also found that the morphological transformation and quenching for low mass galaxies can be two independent processes, suggesting that the interruption of the SF is determined by the halo mass while the morphological transformation is more correlated with the stellar mass.

While to-date the environment plays a big role on the process of star-formation suppression, some recent studies have shown that the environment starts being relevant only at $z < 0.5$ (Hatfield & Jarvis 2017), when the galaxies have already gotten close enough to trigger the ram-pressure stripping, originating a fast quenching process to be added to an existent but slower one, dominated by strangulation (Rodríguez-Muñoz et al. 2019). These two processes start to be important when the galaxy falls into the cluster, i.e. when it crosses the virial radius of a massive cluster (Wetzel et al. 2012), which is a key area to understand the processes regulating the evolution of the galaxy cluster. However, to-date there are still lacking deeper studies of morphological and physical properties of galaxies in clusters, from an homogeneous multi-wavelength point of view (to mention some Liu et al. 2011 and Yan et al. 2014), which is the main goal of this manuscript.

In this work we aim to explore the structural (Sérsic index, effective radius), physical (stellar masses, star-formation rates and colours, etc.) and kinematical properties of galaxies in the Hydra cluster to understand the history and evolution of its galaxies and further extend the knowledge about the effects of the environment over the galaxies. This cluster is a nearby structure located at a distance of ~ 50 Mpc (Misgeld et al. 2011; Arnaboldi et al. 2012) and for which galaxies can be spatially well resolved, making it an ideal laboratory to fulfill our objectives. Hydra is a medium-mass compact cluster (Arnaboldi et al. 2012) with a large fraction of early-type galaxies and at least 50 ultra-compact dwarf galaxies (Misgeld & Hilker 2011; Misgeld et al. 2011). It is classified as a type III structure (Bautz & Morgan 1970), which means it has no dominant central member although there are two bright galaxies near to the centre: NGC 3311, a cD galaxy with radial velocity of 3825 km/s, and NGC 3309, an E3 galaxy with radial velocity of 4009 km/s (Ventimiglia et al. 2011 and references therein). Based on X-ray data, Ventimiglia et al. (2011) have shown evidences that Hydra is a prototype of a dynamically relaxed cluster, showing an isothermal intracluster medium for the most part of the cluster region, indicating that it has not been going through any big merging process during the last few Gyrs (Furusho et al. 2001; Ventimiglia et al. 2011). Given that the cluster virial and X-ray masses are $(5.80 \pm 0.56) \times 10^{14} M_\odot$ and $(9.8 \pm 1.3) \times 10^{14} M_\odot$ respectively, and the global projected velocity dispersion is 660 ± 52 km/s (Babyk & Vavilova 2013) with the centre of the cluster located at ~ 8.6 kpc northeast of NGC 3311 (Barbosa et al. 2018), we will use this galaxy as the central component for practical purposes.

We perform our study from a multiwavelength point of view, by using the wide field (~ 2 sq deg) data of the Southern Photometric Local Universe Survey (S-PLUS; Mendes de Oliveira et al. 2019) and investigate the cluster within $1R_{200}$, the radius at which the mean density is two hundred times the critical density of the Universe. The S-PLUS provides a significant improvement in the understanding of the spectral energy distribution of galaxies at optical wavelengths due to its 12-bands filter system (5 broad and 7 narrow bands), which is a great improvement over most previous studies using up to 8 filters to perform a multi-band fitting. This is the first time that morphological analysis using 12 bands in the visible spectra is presented and the wide field of view of S-PLUS allows us to investigate in great detail any possible

variation in the structural parameters and physical properties as a function of wavelength, cluster-centric distances and density.

This manuscript is presented as follows: in Section 2 we describe the data and how we construct the catalogue of Hydra Cluster galaxies, while in Section 3 we present the methodology used to estimate the structural and physical parameters. In Sections 4 and 5 we present and discuss the results to finally summarise and conclude our work in Section 6. Throughout this study we adopt a flat cosmology with $H_0 = 70$ km s^{-1} Mpc^{-1}, $\Omega_M = 0.3$ and $\Omega_\Lambda = 0.7$ (Spergel et al. 2003).

2 DATA AND GALAXIES CATALOGUE

Observations of the Hydra cluster were taken as part of the S-PLUS by using the T80Cam installed at the 80 cm T80-South telescope located at Cerro Tololo Inter-American Observatory, Chile. The T80Cam has a detector with 9232×9216 10μm-pixels with an effective field of view of 2 square degrees and plate-scale of 0.55 arcsec pixel^{-1}. S-PLUS uses the Javalambre 12-band filter system composed of 5 broad filters (u', g', r', i' and z' – $ugriz$ for simplicity) and 7 narrow-band ones (J0378, J0395, J0410, J0430, J0515, J0660 and J0861) strategically positioned in regions of the electromagnetic spectrum that have important stellar features like [OII], Hα, Hδ, Mgb and Ca triplets (see Table 1 for more information). The S-PLUS filter system was built specifically for stellar classification, yet given its spectral richness, it can also be used to analyse the physical properties of galaxies and planetary nebulae. The survey also provides photometric redshifts for galaxies brighter than 20 mag (in r-band) and $z < 0.5$ (see Molino et al. 2019). The observational strategy was defined to increase depth and reduce noise (the *Petrosian* magnitude limit is $J0395 = 20.11$ – the shallower band – to as deep as $g = 21.79$ with $S/N \geq 3$), while dithering is used to overcome problems with bad pixels (Mendes de Oliveira et al. 2019). A detailed description of the survey including filter system, calibration method (Sampedro et al. in preparation), first results and full assessment of its capabilities can be found in Mendes de Oliveira et al. (2019) where the survey is described.

In this work we use four S-PLUS fields, covering an area of 1.4 Mpc radius, centred on the Hydra cluster, whose central region is shown in Fig. 1. Table 2 lists the central coordinates of each field.

2.1 Kinematic selection of Hydra cluster galaxies

We select all galaxies that are gravitationally bound to the cluster and inside 1 R_{200}. First we select all galaxies with peculiar velocities lower than the cluster escape velocity, which is calculated in the line-of-sight relative to the cluster recessional velocity, as defined by Eq. 1 (see Harrison 1974; Jaffé et al. 2015):

$$pec = c\frac{z - z_{cl}}{1 + z_{cl}} \qquad (1)$$

where $z_{cl} = 0.012$ (Babyk & Vavilova 2013) is the cluster redshift, z is the redshift of each galaxy obtained from the

Table 1. S-PLUS filter system and exposure times for Hydra pointings.

Filter name	λ_{eff} [Å]	$\Delta\lambda$ [Å]	Exp. Time [s]	Comment
uJAVA	3536	352	681	Javalambre u
J0378	3770	151	660	[O II]
J0395	3940	103	354	Ca H+K
J0410	4094	201	177	Hδ
J0430	4292	201	171	G-band
gSDSS	4751	1545	99	SDSS-like g
J0515	5133	207	183	Mgb Triplet
rSDSS	6258	1465	120	SDSS-like r
J0660	6614	147	870	Hα
iSDSS	7690	1506	138	SDSS-like i
J0861	8611	408	240	Ca Triplet
zSDSS	8831	1182	168	SDSS-like z

Figure 1. Hydra central region. Colour composition using the images of the 12 S-PLUS bands with blue corresponding to $u + J0378 + J0395 + J0410 + J0430$, green to $g + J0515 + r + J0660$ and red to $J0861 + i + z$ made using the software Trilogy (Coe et al. 2012).

Table 2. Central position J2000 of the four S-PLUS fields used in this work.

FIELD	1	2	3	4
RA° (J2000)	157.90	159.47	159.30	157.70
DEC° (J2000)	-26.69	-26.69	-28.08	-28.08

NASA/IPAC Extragalactic Database (NED[1]), and c is the speed of light. The cluster escape velocity (v_{esc}), in km/s, is calculated using the Eq. 2 (Eq.1 in Diaferio 1999):

$$v_{esc} \simeq 927 \left(\frac{M_{200}}{10^{14}h^{-1}M_\odot}\right)^{1/2} \left(\frac{R_{200}}{h^{-1}\mathrm{Mpc}}\right)^{-1/2} \qquad (2)$$

The determination of the cluster escape velocity depends on the M_{200} (mass within the R_{200}), R_{200}, which in

---

[1] https://ned.ipac.caltech.edu/

turn are determined by the velocity dispersion (σ), and $h= H_0/100$ km s^{-1} Mpc^{-1}. To obtain σ we use only galaxies with radial velocities ranging from 1800 to 6000 km/s, suggested by Ventimiglia et al. (2011). We found a biweight velocity dispersion of 690 ± 28 km/s as defined by the Eq. 3:

$$\sigma_{BI}^2 = N \frac{\sum_{|u_i|<1} (1 - u_i^2)^4 (v_i - \overline{v})^2}{D(D-1)} \quad (3)$$

where v_i is the peculiar velocity and $\overline{v}$ is its average, as described in Beers et al. (1990a) and Ruel et al. (2014), and N is the number of members. D is given by Eq. 4.

$$D = \sum_{|u_i|<1} (1 - u_i^2)(1 - 5u_i^2) \quad (4)$$

where u_i is defined as shown by Eq. 5.

$$u_i = \frac{v_i - \overline{v}}{9\text{MAD}(v_i)} \quad (5)$$

and MAD(v_i) is the median absolute iation of the velocities. The biweight velocity dispersion uncertainty is calculated as given by Eq. 6.

$$\Delta\sigma_{BI} = \frac{C_{BI}\sigma_{BI}}{\sqrt{N-1}} \quad (6)$$

where $C_{BI} = 0.92$. After measuring σ (690 ± 28 km/s in our case), we can use it to determine M_{200} and R_{200} following Leonard & King (2010). They use a singular isothermal sphere model profile, assume spherical symmetry, and that the 3D velocity dispersion can be described from the line-of-sight one dimensional velocity dispersion (Gonzalez et al. 2018). The relationship found by Leonard & King (2010) between σ, M_{200} and R_{200} is as follows:

$$M_{200} = \frac{2\sigma^3}{\sqrt{50}GH} \quad (7)$$

$$R_{200} = \frac{\sigma}{\sqrt{50}H} \quad (8)$$

where G and H are the gravitational and Hubble constants, respectively. We find a $M_{200} = 3.1 \pm 0.4 \times 10^{14} M_\odot$ and $R_{200} = 1.4 \pm 0.1$ Mpc. We also calculate M_{200} using the relation between velocity dispersion and M_{200}, as obtained by Munari et al. (2013) for simulated galaxy clusters, and described by Eq. 9.

$$\frac{\sigma_{D1}}{\text{km s}^{-1}} = A_{1D} \left[\frac{h(z)M_{200}}{10^{15}M_\odot} \right]^\alpha \quad (9)$$

The values of A_{1D} and α for the Eq. 9 are found in Munari et al. (2013). The velocity dispersion in the simulation is determined using Dark Matter particles (DM), subhaloes (SUB) and galaxies (GAL). The three cases consider the contribution of AGN feedback. Using the Eq. 9 we obtained the following M_{200} masses, in units of $10^{14} M_\odot$, for DM, SUB and GAL, respectively, 3.5 ± 0.4, 3.1 ± 0.3 and 3.3 ± 0.3, which are in agreement with M_{200} estimated using Eq. 7, as well as other reported values (e.g. $M_{200} = 3.8 \times 10^{14}$ from Comerford & Natarajan 2007).
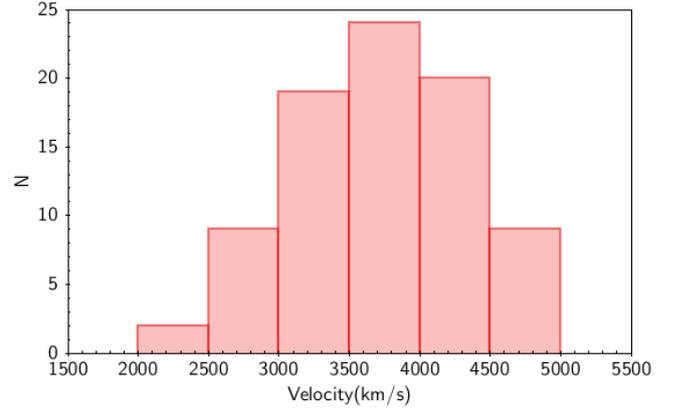

Figure 2. Histogram of the velocity distribution for the 81 Hydra Cluster galaxies of our sample. The y-axis shows the number of galaxies at each velocity bin.

Using the calculated $M_{200} = 3.1 \pm 0.4 \times 10^{14} M_\odot$ and $R_{200} = 1.4 \pm 0.1$ Mpc, we obtain $v_{esc} = 1379$ km/s from Eq. 2, which gives us a sample of 193 galaxies satisfying the criteria to be members of the Hydra Cluster within 1 R_{200}. To check our consistency, we use another method to select Hydra members by applying a 3 sigma-clipping to the recessional velocity distribution of the galaxies. For this, we reject galaxies with recessional velocities larger than 3σ which results in a sample of 223 objects located within 1 R_{200}.

Although both methods provide numbers of cluster members within the same order of magnitude, ensuring that our choice will not affect the results of this paper, we will use the sample selected by the first method to ease further comparisons with other studies.

2.2 Final complete sample of Hydra galaxies

In order to produce a complete galaxy sample in Hydra, we performed a cross match between different spectroscopic surveys in the Hydra area from Richter (1987); Stein (1996); Jones et al. (2004). All these spectroscopic studies are complete for galaxies brighter than ~ 16 mag in the r-band. Therefore, in this study we only include the selected galaxies in sect. 2.1 that are brighter than 16 mag in the r-band, to ensure a complete sample of galaxies analysed. Given this, all galaxies analysed here have large S/N, between 24 and 145 (in the r-band) with a mean value of 55.

We note that some of the galaxies of our sample were not well fitted by MegaMorph (see Section 3.1) due to either foreground stars contamination or to its proximity to the CCD edge. After removing these objects we obtain a final sample of 81 galaxies brighter than 16 (r-band), within 1 R_{200}, and with peculiar velocities lower than $v_{esc} = 1379$ km/s. We use these galaxies to analyse the behaviour of the morphological parameters, for example Sérsic index. Figures 2 and 3 show the distribution of recessional velocities and a colour-magnitude diagram (CMD) respectively, for the selected 81 galaxy members. We note, in Fig. 3, that most galaxies are located in the red sequence, and there is a clear relation between the Sérsic index and the galaxy's colour, redder galaxies have a higher Sérsic index.
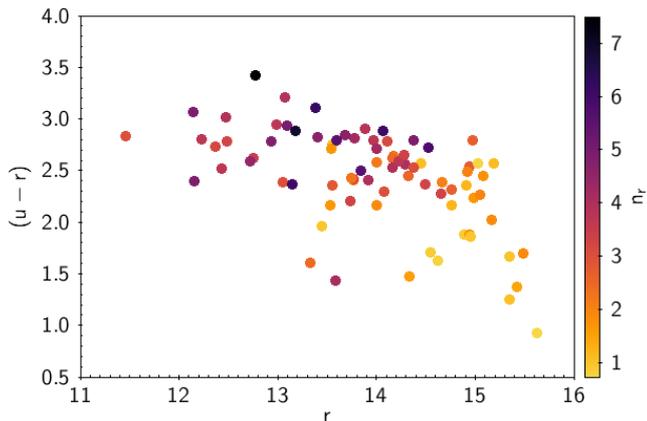
Figure 3. Colour magnitude diagram for the galaxies in Hydra Cluster. The dots are colour-coded by the Sérsic index in the r-band. Most of the galaxies are located within the red sequence. There is a clear relation between the Sérsic index and the galaxy's colour.

3 METHODOLOGY

3.1 Morphological Parameters

The morphological classification of galaxies can be done by visual inspection (e.g., Lintott et al. 2008; Kartaltepe et al. 2015; Simmons et al. 2017). It is, however, extremely costly on human resources to perform over millions of galaxies which are available within modern surveys. For this volume we must rely on the computational power we have available and use a different approach to obtain the structural parameters of galaxies, such as Sérsic index (n), effective radius (R_e), bulge-to-total Flux (B/T), Gini coefficient and the second-order moment of the brightest 20 percent of the galaxy (Lotz et al. 2004). All these parameters can be used to classify galaxies morphologically, specially considering that morphological analyses can be done from the infrared to the ultraviolet regions of spectra (Gil de Paz et al. 2007; Lotz et al. 2008; Wright et al. 2010; Dobrycheva et al. 2017). Indeed, the Sérsic profile describes how the intensity of a galaxy varies with radius, providing information regarding the morphology of the galaxy (Sérsic 1963). This is the approach we adopt in this work, whose motivation is two folded: on one side, automatic classification allows us to consider a morphological analyses from the infrared to the ultraviolet regions of spectra, done in a consistent way. On the other hand, it will allow us to readily compare our results with future S-PLUS and J-PLUS data, which will deliver multiband data for millions of galaxies (Mendes de Oliveira et al. 2019), as well as with other work, that have also performed automatic classification.

With the purpose of estimating the Sérsic index (n), effective radius (R_e) and the magnitudes (m) for the members of the Hydra Cluster in all S-PLUS bands, we used the code MegaMorph-GALAPAGOS2 (Bamford et al. 2011; Vika et al. 2013; Häußler et al. 2013). This code performs a multiwavelength two-dimensional fitting using the algorithm GALFITM (Peng et al. 2002, 2010a; Vika et al. 2013). GALFITM extracts structural components from galaxy images by modelling the surface-brightness with different profiles: Nuker law (Lauer et al. 1995), the Sérsic profile, ex-

ponential disc, Gaussian or Moffat functions (Moffat 1969). The main advantage of a simultaneous multiwavelength fitting is an increasing in the accuracy of the estimated parameters (Vika et al. 2015). In addition, MegaMorph allows us to fit all galaxies in a given field simultaneously, which is of great convenience. We note that MegaMorph was used to perform a multiband fitting in several previous studies (Vika et al. 2013, 2014, 2015; Häußler et al. 2013; Vulcani et al. 2014; Kennedy et al. 2015; Dimauro et al. 2018). In addition, it was tested with simulated galaxies (Häußler et al. 2013). Thus it is a well-tested code. The galaxies analysed here have large S/N, between 24 and 145 (in the r-band) with a mean value of 55, and good imaging quality, since all images were taken under photometric conditions; thus we trust that the output parameters provided by MegaMorph are reliable. Nevertheless, as a sanity check, we tested how well GALFITM recovers the galaxy parameters for our particular data set of S-PLUS. We present this test in the Appendix B, where we generate simulated galaxies with the same features, S/N, filters and background levels as those in the S-PLUS fields of Hydra, and find that GALFITM can retrieve the input galaxy's parameters with high reliability, within a percentage error of ~ 4 percent (see Appendix B for more details).

In this work, the centre of each galaxy was determined by SourceExtractor using a deep detection image, generated for each field as a weighted combination of the g, r, i and z broad-band images. Then, for each galaxy, we fit a single Sérsic profile simultaneously for images in all filters, by fixing for each filter the central position measured on the detection image. Each parameter to be measured is modeled as a function of wavelength and the degrees of freedom afforded to model each of these parameters is determined by a set of Chebyshev polynomials. This analysis provided us structural parameters, such as the Sérsic index and effective radius (modelled as quadratic functions of wavelength) as well as b/a and position angle (modelled as linear functions of wavelength) Häußler et al. (2013). The Sérsic profile, which is modeled for each galaxy, is define in Eq. 10.

$$I(r) = I_e \left\{ -b_n \left[\left(\frac{r}{R_e} \right)^{\frac{1}{n}} - 1 \right] \right\} \qquad (10)$$

where I_r is the intensity, R_e and I_e are the effective radius and the intensity inside an R_e, respectively. n is the Sérsic index, also known as the concentration parameter, and b_n is a function of n that satisfies $\Gamma(2n) = 2\gamma(2n, b_n)$. In cases where the galaxy profile is more concentrated, n presents higher values. For instance, with $n = 4$ we obtain the well known de Vaucouleurs profile and it corresponds to the typical profile of an elliptical galaxy. For $n=1$, we have a typical profile of an exponential disk, and if $n < 1$ this is probably due to the presence of a bar (Peng et al. 2010a).

In order to determine the best fit, GALFITM uses a Levenberg-Marquardt technique, which finds the optimum model by minimising the chi^2. In Fig. 4 we present the GALFITM output for the galaxy ESO 437- G 004, as an example, where observed images, models and residuals (observed minus models) are shown in top, middle and bottom panels, respectively. We can easily see the spiral arms and substructures in the residual images of this example.

Magnitudes and Sersic index for the 81 analysed galax-

ies are available in Tables A1 and A2 (see Appendix B for a complete version of these tables). All magnitudes used in this work have been corrected for Galactic extinction, by using a Cardelli et al. (1989) law and the maps from Schlegel et al. (1998).

3.2 Estimation of stellar masses

3.2.1 Stellar mass from colours

The stellar mass is one of the main properties of a galaxy and it is well correlated with its luminosity (Faber & Gallagher 1979). Different types of galaxies increase their stellar masses at different rates, starburst galaxies form stars at higher rates than main sequence galaxies (Papovich et al. 2005). Bell et al. (2003), using a large sample of 22,679 galaxies observed with the Two Micron All Sky Survey (Skrutskie et al. 1997) and the SDSS, calculated stellar mass-to-light ratio $M_\star/L$ as a function of the colour $(g - i)$ assuming a Salpeter initial mass function (IMF, Salpeter 1955). In this work we use the i-band luminosities, along with the colour $(g - i)$, to estimate the stellar mass following the definitions given by Bell et al. (2003), which are shown in the Eqs. 11.

$$\log \ M_\star/L_i = -0.152 + 0.518 \times (g - i) \tag{11}$$

We found a median uncertainty of 0.06 dex for the estimated stellar masses of our Hydra galaxies. Using a sample of galaxies from the Galaxy And Mass Assembly (GAMA), Taylor et al. (2011) have shown that the colour $(g - i)$ can be used to infer $M_\star/L_i$ with a typical uncertainty of < 0.1 dex following the definition shown in Eq. 12

$$\log \ M_\star/L_i = 1.15 + 0.7 \times (g - i) - 0.4 \times M_i \tag{12}$$

where M_i is the absolute magnitude in the i-band. The authors used the SSPs models from Bruzual & Charlot (2003) and assumed a Chabrier (2003) IMF with a Calzetti et al. (2000) extinction law. In this work we also use the relation presented in Taylor et al. (2011) to estimate the stellar masses.

3.2.2 Stellar mass using LePHARE

Another way to estimate the stellar mass of a galaxy is using a Spectral Energy Distribution (SED) or spectral fitting code (Bruzual A. & Charlot 1993; Cid Fernandes et al. 2005; da Cunha et al. 2012). These codes use models to fit the SED, allowing us to determine the ages and metallicities of the stellar populations. Then, it is possible to obtain several physical parameters of the galaxy, including its stellar mass.

Following this approach, we perform a SED fitting for the galaxies detected inside of the S-PLUS field containing the centre of the Hydra Cluster (only one field for a consistency check). The SED fitting process was done using the code PHotometric Analysis for Redshift Estimate (LePHARE Arnouts et al. 1999; Ilbert et al. 2006) and the stellar population libraries of Bruzual & Charlot (2003) with a Chabrier (2003) IMF. The models have 3 metallicities $0.2 Z_\odot$, $0.4 Z_\odot$ and $1 Z_\odot$ with age ranging from 0.01 to 13.5 Gyrs.

In Fig. 5 we compare the resulting masses obtained by the SED fitting method with respect to the masses derived from luminosities and colours (as described in Section 3.2.1). Red dots are the stellar masses estimated using the colour relation $(g - i)$ from Bell et al. (2003). We have scaled the Bell mass-luminosity relation by 0.093 dex to take into account the use of Salpeter IMF rather than a Chabrier IMF, as described in Taylor et al. (2011). Blue dots are the stellar masses estimated using the colour relation $(g - i)$ from Taylor et al. (2011). The stellar masses estimated using Bell et al. (2003) are on average 0.22 dex larger than those estimated via Taylor et al. (2011). When the stellar masses derived from the SED fitting are compared with those derived from the colour relations we find, on average, a percentage error of 1.2 and 2.0 for the masses estimated using the Taylor et al. (2011) and Bell et al. (2003) relations, respectively. In both cases a linear regression of the stellar masses obtained from the two methods provides a good fit, with a coefficient of determination $R^2 = 0.97$, indicating a good lineal correlation between the data. The coefficient of determination is defined as $R^2 = 1 - (SS_{res}/SS_{tot})$, where SS_{res} is the sum of residual errors and SS_{tot} is the total errors. Its value ranges from 0 to 1, where 1 corresponds to the maximum correlation.

Given that the two colour relations show a good correlation with the masses estimated using a SED fitting, and considering that the masses estimated using colours is less time consuming, we therefore use the stellar masses for all the S-PLUS fields obtained from the colour relation by Taylor et al. (2011), which shows the smallest percentage error.

We show the stellar mass function (SMF) of the Hydra galaxies analysed in this work as a grey histogram in Fig. 6. The SMF is dominated by ETGs and quenched galaxies, as defined in the following sections. Our sample is complete for stellar masses $\geq 3.3 \times 10^9 M_\odot$, which was determined from the colour relation using the faintest magnitude (16 mag in the r-band) and the reddest colour of our sample of galaxies. We can see from Fig. 6 that there are virtually no ETGs and quenched galaxies (NSFG) in the lower mass end of the SMF. The stellar masses are listed in Table A3 of the Appendix.

3.3 The star formation rate estimation

To further extend our understanding of the galaxies inside the Hydra Cluster and the influence of the environment over the evolutionary path of the members, we estimate the star formation rate (SFR) and the specific star formation rate $(sSFR)$ for the galaxies of our sample. For this task we use the $J0660$ narrow band filter, which is centred around the rest frame wavelength of Hα. We note that there are several advantages in using photometric data to determine Hα emission in galaxies. First, the use of S-PLUS data allow us to perform an homogeneous analysis on the Hα emission of galaxies in Hydra, where all the data were observed under similar conditions. In addition, imaging surveys are not biased by the orientation of the slits, as in the case of spectroscopic studies. Furthermore, the S-PLUS will cover a huge area in the sky, and in the near future the photometric redshifts will be available, increasing the number of objects belonging to Hydra for which we will have S-PLUS data. In this way, the same criteria will be used to select and analyse galaxies providing homogeneous data with S-PLUS.

We select the emission line galaxy candidates in our
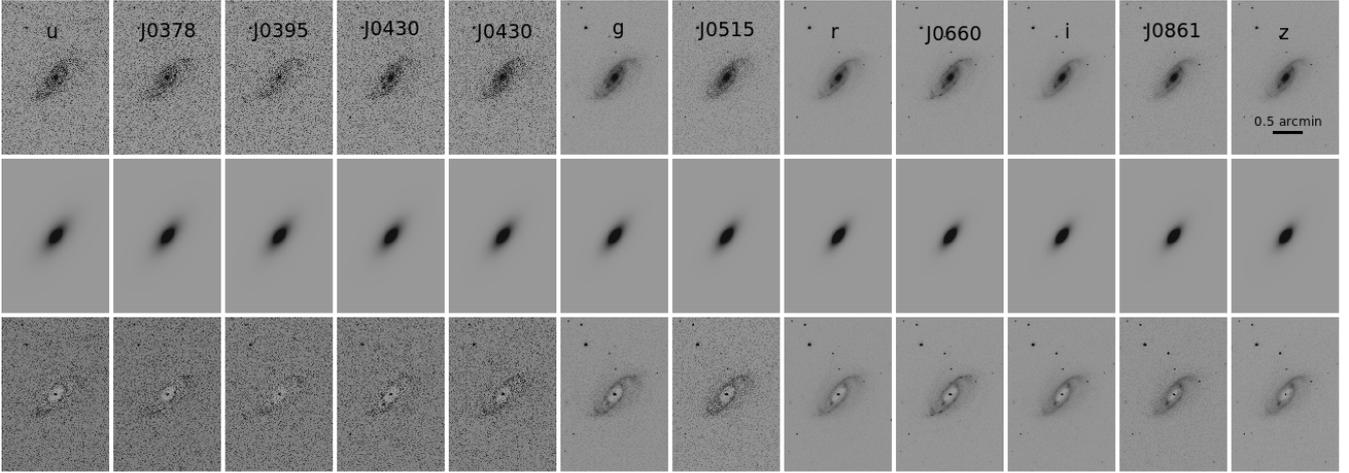
Figure 4. Galaxy ESO 437-G 004 as observed by S-PLUS (top panels), the models calculated using GALFITM (middle panels), and the residual image (observed minus modelled – bottom panels).
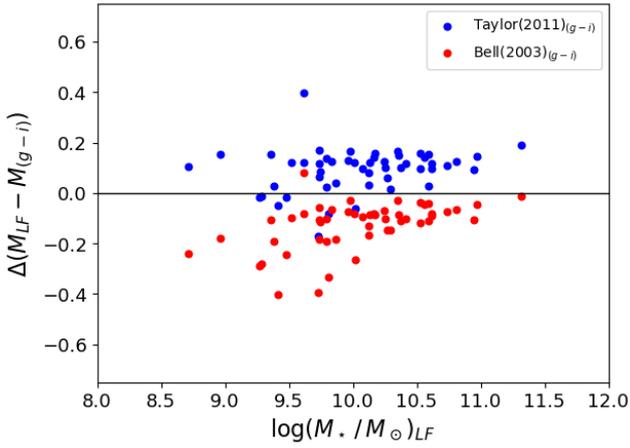

Figure 5. Comparison between the stellar masses estimated using colours and using the code LePHARE. The y-axis shows the difference between the stellar masses calculated with LePHARE and colour relation. In red and blue are the masses estimated using the colour $(g - i)$ from Bell et al. (2003) and Taylor et al. (2011), respectively.

Figure 6. Stellar mass function of galaxies brighter than m_r=16 within a sphere with 1.4Mpc of radius centred on Hydra. The grey line is the 81 galaxies belonging to Hydra selected as indicated in subsection 2.1. The orange and cyan lines are the quenched (NSFGs) and SFGs. The red and blue lines are ETGs and LTGs respectively.

sample based on two criteria: one regarding the equivalent width and the other one regarding a given colour excess for the objects (known as 3Σ cut). For the galaxies to be considered as line emitters, the H_α equivalent width (EW_{J0660}) should be greater than 12 Å. This is following Vilella-Rojo et al. (2015), who determine that J-PLUS cannot resolve, with a precision of 3σ, EW_{J0660} < 12 Å. In this work, we use the same criteria given that S-PLUS and J-PLUS use twins telescopes, with the same filters systems, thus we can utilize the same criteria to analyse the galaxies if the ob-

jects have the similar photometric conditions. We use the equation 13 to determine the galaxies's EW_{J0660}.

$$EW_{J0660} = \Delta_{J0660}(Q - 1)\frac{Q - 1}{1 - Q\epsilon} \qquad (13)$$

where $\epsilon \equiv \Delta_{J0660}/\Delta_r$ and m_r - $m_{J0660} = 2.5 \log Q$. The m_r and m_{J0660} are the apparent magnitudes.

Emission line galaxies are objects with colour excess

(15)
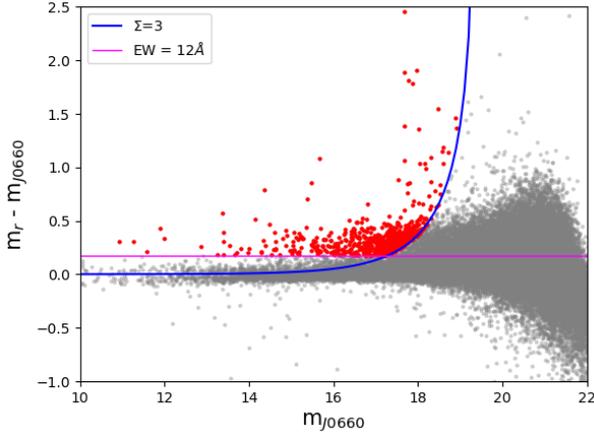
Figure 7. m_{J0660} excess as a function of m_{J0660} magnitude. The blue line represent the Σ cut of 3. The magenta horizontal line present the EW_{J0660} cut of 12 Å. The grey points represent all $m_r - m_{J0660}$ detected sources. The red points are the sources that can be considered to have a narrow-band excess in the field.

greater than zero (r - J0600) > 0. However, to quantify the colour excess when compared to a random scatter expected for a source with zero colour, we use a 3Σ cut (Sobral et al. 2012). We use Eq. 14 to define the 3Σ curve (Khostovan et al. 2020) for our second selection criterion

$$\Sigma = 1 - \frac{10^{-0.4(m_r - m_{J0660})}}{10^{ZP - m_{J0660}}\sqrt{\sigma_{J0660}^2 + \sigma_r^2}} \quad (14)$$

where σ_{J0660} and σ_r are the rms error. SourceExtractor (Bertin & Arnouts 1996) was used in this case to obtain the galaxy magnitudes, and their errors, for each Hydra's field, with a AUTO aperture around the source. ZP is the photometric zero-point for J0660 filter. Figure 7 shows the application of these selection criteria to the detected sources in one Hydra field. Only galaxies that obey the 3Σ cut and $EW_{J0660} > 12$ Å were selected as line emitters. We apply the same selection on all 4 S-PLUS fields analysed in this work and find only 10 galaxies in Hydra that meet our selection criteria to be emission line galaxy candidates. These galaxies have H_α luminosities between 1.4×10^{40} and 1.5×10^{41} erg/s.

To measure the Hα flux on the emission-line selected galaxies, we apply the Three Filter Method (TFM Pascual et al. 2007) – which has already been successfully implemented to similar data from the J-PLUS survey (Cenarro et al. 2019; Vilella-Rojo et al. 2015) – using the r and i-bands to trace the linear continuum and $J0660$ to contrast the line. We obtain a "pure" Hα plus [NII] doublet emission. Even though it is impossible to separate the contribution of the [NII] lines from the Hα flux, given the width of the $J0660$ filter, we can use the empirical relations from Vilella-Rojo et al. (2015) to estimate the level of contamination one could expect in such kind of data. Following the relations from the Eq. 15, we are able to subtract the contribution of [NII] for the flux and obtain a pure Hα emission for our galaxies.

$$\log F_{H\alpha} = \begin{cases} 0.989 \log F_{H\alpha+[NII]} - 0.193, & \text{if } g - i \leq 0.5 \\ 0.954 \log F_{H\alpha+[NII]} - 0.753, & \text{if } g - i > 0.5 \end{cases}$$

The analysis described above allow us to determine a sensitivity of the $F_{H\alpha}$ is 1×10^{-13} erg s^{-1}cm^{-2} which corresponds to a surface brightness of 21 mag/arcsec^{-2}. We use the Hα flux to determine the Hα luminosity, and then the classical relation proposed by Kennicutt (1998) was used to estimate the SFR. The SFRs obtained from this relation must be corrected for dust attenuation. A common correction arises from the assumption of an extinction A(Hα) = 1 mag, as proposed by Kennicutt (1992). However, this correction overestimates the SFR for galaxies with low Hα luminosities (Hα luminosity of $< 10^{40.5}$ ergs s^{-1}, Ly et al. 2012), which is the case for some galaxies analyzed in this work. For these reasons, we choose to use the relation between the intrinsic and observed SFR (corrected by the obscuration), which is presented in Hopkins et al. (2001) and updated by Ly et al. (2007). The relation is shown in Eq. 16.

$$\log SFR_{obs}(H_\alpha) = \log SFR_{int} - 2.360$$
$$\times \log \left[\frac{0.797 \log(SFR_{int}) + 3.786}{2.86} \right] \quad (16)$$

where SFR_{int} and SFR_{obs} are the intrinsic and observed SFR respectively.

Finally, $sSFR$ were estimated by using SFR and the stellar masses derived in section 3.2.1. Table A3 in the appendix lists the $sSFR$ (column 6). A $sSFR$ threshold is defined empirically to separate star-forming galaxies (SFGs) from the non-star forming ones (NSFGs Weinmann et al. 2010). We consider a galaxy as star-forming if its $sSFR > 10^{-11}$ yr^{-1} otherwise it will be classified as quiescent following the threshold commonly used in the literature (see for example Wetzel et al. 2012, 2013, 2014). We note, however, that some other studies use different thresholds for the $sSFR$ at different redshifts to separate SFG from NSFG, as for example Laganá & Ulmer 2018 and Koyama et al. 2013. Based on these definitions we found that the Hydra cluster has 88 percent of the galaxies already quenched.

4 RESULTS

In this section we present the morphological classification of Hydra galaxies as early and late-type galaxies using n and colours. We then analyse the spatial distribution of the different types of galaxies in terms of their physical and structural parameters as well as their behaviour with respect to the cluster central distance and with the cluster density. We also present the n behaviour as a function of the 12 S-PLUS filters. In addition, we analyse the phase-space diagram and we explore the presence of substructures in Hydra cluster

4.1 Early-type and late-type galaxies classification

Based on the physical properties of the stellar populations of ETGs and LTGs, it is straightforward to separate between these two populations using a colour-magnitude diagram (Bell et al. 2004). ETGs have in general much older and redder stellar populations, which allocates this population in a very well determined position of the diagram separated from the bluer and star-forming LTGs (Lee et al.
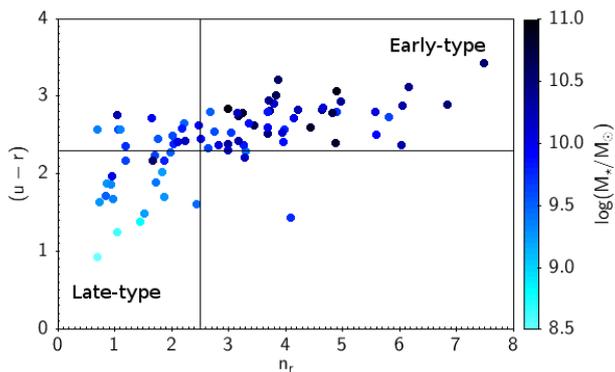
Figure 8. Results of the morphological fitting, performed with MegaMorph-GALAPAGOS2. The x-axis shows the Sérsic index in the r-band the y-axis displays the galaxies' $(u - r)$ colour. Colours represent the stellar mass of each galaxy, as indicated by the colour bar. The vertical and horizontal lines are in $n_r = 2.5$ and $(u - r) = 2.3$, respectively.

2007). Using *SDSS* data Vika et al. (2015) combined n_r and the colour cut $(u - r) = 2.3$ to separate these two galaxy classes (see also Park & Choi 2005 for different values of the colour cut). Vika et al. (2015) classified the galaxies with $(u - r) \geq 2.3$ and $n_r \geq 2.5$ as ETGs and galaxies with $(u - r) < 2.3$ and $n_r < 2.5$ as LTGs. Following these parameters to classify our sample, ~ 54 percent of the galaxies (44 objects) are ETGs, whereas ~ 23 percent (19 galaxies) are LTGs.

In Figs. 8 and 9 we present the n_r versus the $(u-r)$ colour for the whole sample used in this study, where symbols in the figures are colour-coded by stellar mass and sSFR, respectively. As expected, ETGs (top-right region on each plot) are more massive than LTGs (bottom-left region). In Fig. 9, we show that LTGs are forming stars at a level of -10.0<log(sSFR)<-8.8 whereas all the ETGs are quenched. It is interesting to note that there is a population of blue + green galaxies $((u - r) < 2.3)$ in Hydra cluster that do not present $H\alpha$ emission at the detection level. The SMF of SFGs and NSFGs is shown in the Fig. 6, as cyan and orange histograms respectively. We find that the SFGs are less massive than the NSFGs, where the NSFG have basically the same behaviour of the global SMF, since only 10 galaxies of the sample are SFGs. There is a mix of populations in the top left in the Figures 8 and 9, which represents a ~ 17 percent of our sample.

4.2 Spatial distribution: structural and physical parameters

In this section we analyse how the morphological and physical parameters change with respect to the distance to the cluster centre as well as a function of the projected local density. For each galaxy we estimate the projected local density defined as $\Sigma_{10} = 10/A_{10}$, where $A_{10} = \pi R_{10}^2$(Mpc) is the area of the circle that contains the nearest 10 galaxies and R_{10}^2 is the radio of the circle, as described by Fasano et al. (2015). Each galaxy is in the centre of the circle.

The top panel of Fig. 10 shows the spatial distribution of ETGs and LTGs classified in subsection 4.1. The red and blue dots are the ETGs and LTGs respectively, and the grey dots are the mix of galaxies that do not meet the ETG or
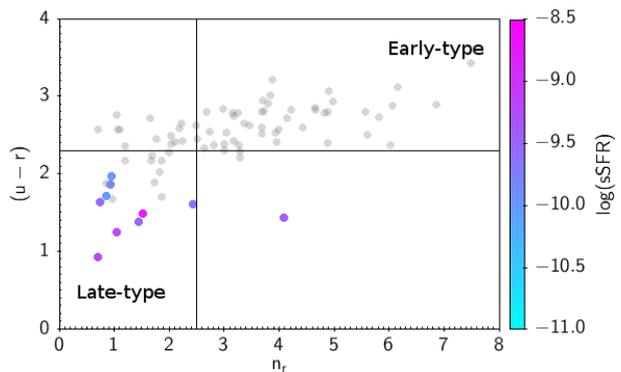
Figure 9. Same as Fig. 8, but colour-coded by the $log(sSFR)$. The grey dots are NSFG.

LTG definition requirements (first and fourth quadrants in Fig. 8). The size of each circle is proportional to the n_r. The middle and bottom panels show the radial fraction and histograms of ETGs and LTGs, respectively. The fractions are calculated over the total number of galaxies. We find that the fraction of ETGs is higher than the LTGs fraction, basically for all bins, except at $\sim 0.9 R_{200}$, where the behaviour is inverted. We find that ~ 47 percent of the LTGs and ~ 75 percent of the ETGs are inside $0.6 R_{200}$. The number of LTG and ETG galaxies beyond $0.6 R_{200}$ is quite similar.

Figure 11 shows the radial fraction and histograms for n_r, $(R_{e,z}/R_{e,g})$ and SFG, NSFG with respect to the clustercentric distance. Panels a and b show that most galaxies (~ 59 percent) have $n_r \geq 2.5$, and their fraction (panel a) is higher than that of galaxies with $n_r < 2.5$ up to $\sim 0.5 R_{200}$, after that the fractions are basically the same for the two groups of galaxies.

The c and d panels of Fig. 11 show the ratio of effective radii in z and g bands $(R_{e,z}/R_{e,g})$. Hydra has 40 galaxies with $(R_{e,z}/R_{e,g}) > 1$ and 41 otherwise, showing a similar fraction for these two cases across R_{200}.

Panels e and f of Fig 11 show the fraction and radial distribution of SFGs and NSFGs. We find that ~ 88 percent of galaxies in Hydra (71 galaxies) are quenched. These quenched galaxies are found at all distances from the cluster centre, however their number decreases as a function of clustercentric distance. We also find that there are no SFGs in the central bin, i.e. inside $\sim 0.3 R_{200}$ of Hydra. Owers et al. (2019), who studied a sample of galaxy clusters at low redshift, also found that the number and the fraction of passive galaxies decrease towards larger clustercentric distances. They found that beyond $0.3 R_{200}$ the number of SFG remains relatively constant, while the fraction of SFGs increases as a function of clustercentric distance. Pallero et al. (2019) studied a sample of galaxy clusters from the EAGLE hydrodynamical simulation. They classified SFGs as we do in this work, i.e. galaxies with log(sSFR) > -11, and found that a cluster as massive as Hydra (M_{200} >$3\times10^{14}M_\odot$) has ~ 90 percent of the galaxies quenched, in agreement with our findings.

We show in Fig. 12 the distribution of SFGs and NSFGs as a function of projected local density. No SFGs are found in the highest and lowest density bins. The NSFGs dominate at all densities, however after $\sim \log(\Sigma_{10} > 1.2)$ the fraction of NSFG increases towards denser regions, while the fraction
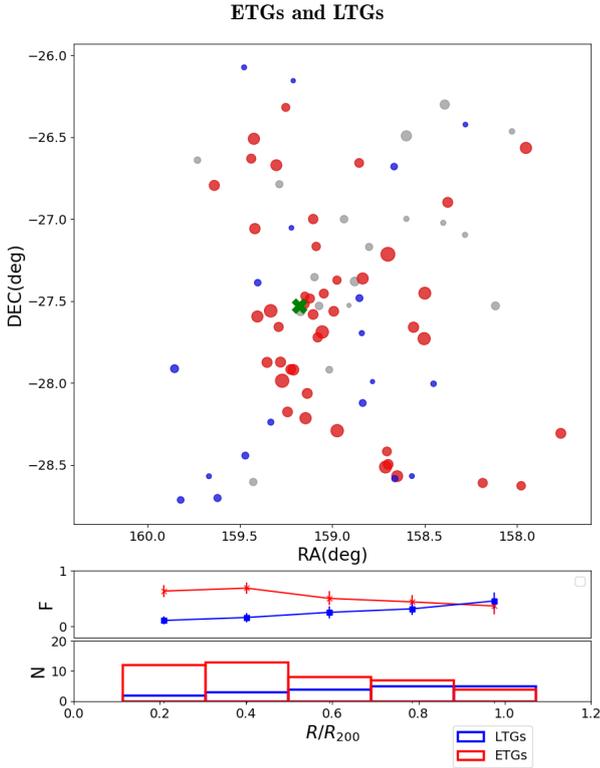
ETGs and LTGs

Figure 10. Top panel: Hydra's galaxies distribution. The x-axis shows the RA and y-axis shows the DEC in degrees. The radial extension is from the centre up to $\sim R_{200}$. The blue and red dots are the LTGs and ETGs respectively. The grey dots are the galaxies in the first and fourth quadrants in the Fig. 8. The size of each circle is proportional to the n_r. The green x symbol is the cluster centre. Middle panel shows the fraction of LTGs and ETGs in blue and red respectively, as a function of distance in terms of R200. Bottom panel: histogram of galaxies per R_{200} bin.

of SFG decreases in the same direction. The error bars in Figures 10, 11 and 12 are binomial uncertainties with a 68 percent confidence.

4.3 Behaviour of n as a function of the 12 S-PLUS filters

The light emitted by a galaxy at different wavelengths has information from different physical phenomena. As an example, stellar populations of different ages and metallicities have emission peaks in different regions of the spectrum. In addition, other contributions such as emission from HII regions, AGN, and planetary nebulae can also be found in a galaxy spectrum. In the case of S-PLUS, each filter is placed in optical strategic regions. Thus, within this context, it is interesting to measure how n changes with respect to each S-PLUS filter, clustercentric distance and density. In order to investigate it, we separate the Hydra galaxies into four groups: i) ETG, ii) LTG, iii) red and iv) blue + green, to facilitate comparisons with other studies. Galaxies with $(u-r) \geq 2.3$ are red (58 galaxies) and galaxies with $(u-r) < 2.3$ are blue + green (23 galaxies). ETGs and LTGs follow the definition provided in Section 4.1. Fig. 13 shows how the median Sérsic index $(\bar{n})$ changes as a function of wavelength. The $\bar{n}$ for red galaxies shows a larger value (13 percent) toward redder filters. The $\bar{n}$ for blue + green galaxies remains
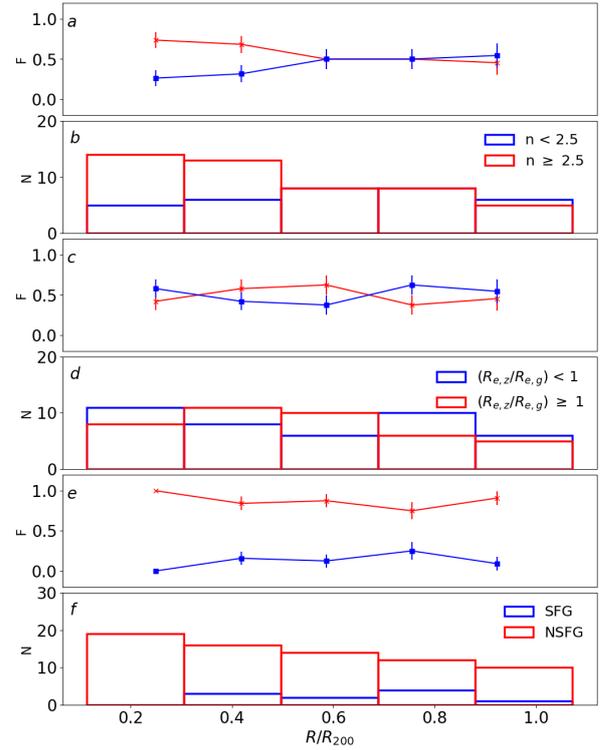
Figure 11. The fraction (F) and histogram representing the number of galaxies (N) per R_{200} bin. Panels a and b show galaxies with $n_r \geq 2.5$ and < 2.5 in red and blue respectively. Panels c and d show galaxies with $(R_{e,z}/R_{e,g}) \geq 1$ and < 1 in red and blue respectively, finally panels e and f show NSFG and SFG in red and blue respectively.
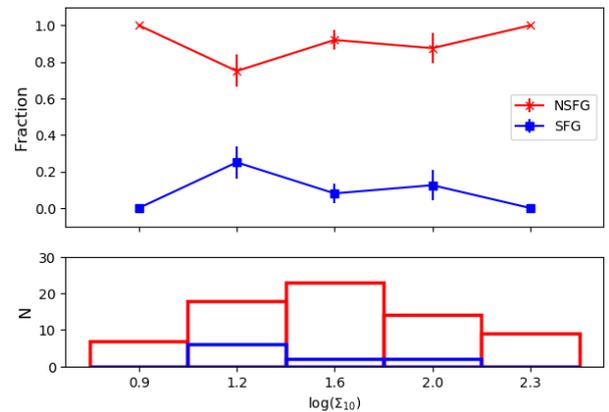
Figure 12. SF and NSF-Density relation. Top panel: fraction of SFG and NSFG in blue and red, respectively. Bottom panel: Histograms with the number of galaxies per density bin.

constant across all filters. For ETGS, $\bar{n}$ increases with wavelength (18 percent), whereas for LTGs it decreases up to the $J0515$-band, and after that increases its value up to z-band. The LTGs present a net decrease, from filter u to z, of 7 percent. The $\bar{n}$ values and their uncertainties per filter, estimated by adding the individual uncertainties in quadrature and dividing by the number of galaxies, for ETGs, LTGs, red and blue + green galaxies are in Table 3.

Table 3. Median of Sérsic index ($\bar{n}$) of the galaxies per filter. The errors were estimated by adding the individual uncertainties in quadrature, divided by the number of galaxies per filter.

GALAXIES	$\bar{n}_u$	$\bar{n}_{J0378}$	$\bar{n}_{J0395}$	$\bar{n}_{J0410}$	$\bar{n}_{J0430}$	$\bar{n}_g$	$\bar{n}_{J0515}$	$\bar{n}_r$	$\bar{n}_{J0660}$	$\bar{n}_i$	$\bar{n}_{j0861}$	$\bar{n}_z$
ETG	3.31±0.03	3.52±0.02	3.55±0.02	3.56±0.02	3.57±0.01	3.62±0.01	3.69±0.01	3.87±0.01	3.91±0.01	4.02±0.01	4.05±0.01	4.06±0.01
LTG	1.74±0.02	1.66±0.01	1.60±0.01	1.54±0.01	1.46±0.01	1.32±0.01	1.27±0.01	1.45±0.01	1.47±0.01	1.56±0.01	1.62±0.01	1.62±0.01
RED	3.21±0.03	3.22±0.02	3.22±0.02	3.24±0.01	3.23±0.01	3.33±0.01	3.41±0.01	3.58±0.01	3.62±0.01	3.72±0.01	3.72±0.01	3.70±0.01
BLUE + GREEN	1.80±0.02	1.72±0.02	1.73±0.01	1.74±0.01	1.72±0.01	1.70±0.01	1.67±0.01	1.68±0.01	1.71±0.01	1.74±0.01	1.75±0.01	1.72±0.01
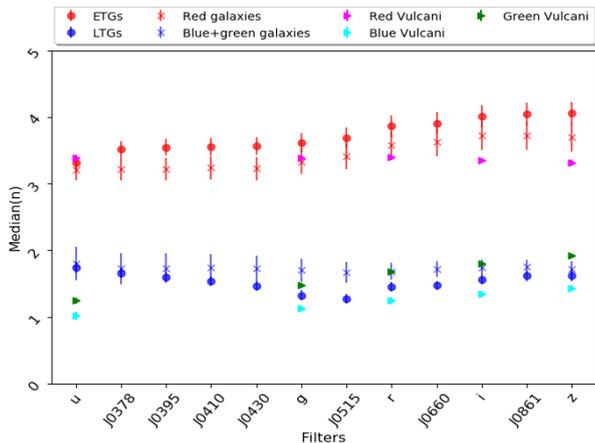
Figure 13. Median Sérsic index $\bar{n}$ as a function of the 12 S-PLUS filters. Red symbols represent ETGs and red (($u-r$) $\geq$2.3) galaxies, blue symbols represent LTGs and blue + green (($u-r$) < 2.3) galaxies. The error bars are the standard error of the median $1.253\sigma/\sqrt{N}$, where N is the number of objects. **The magenta, green and cyan symbols are the red (u-r $\geq$ 2.1), green (1.6 > (u-r) < 2.1), and blue (u-r $\leq$ 1.6) galaxies in** Vulcani et al. (2014); **see Section 5 for more details.**

Figures 14 and 15 show how $\bar{n}$, for each S-PLUS filter, changes with density (quantified by $\log(\Sigma_{10})$) for red and blue + green galaxies, respectively. The $\bar{n}$ for red galaxies (Fig. 14), shows an increase up to $\log(\Sigma_{10}) = 1.6$, and then decreases for denser regions. For the blue + green galaxies (Fig. 15) $\bar{n}$, in general, remains nearly constant at all densities.

Figures 16 and 17 show the behaviour of $\bar{n}$ for each filter, for red and blue + green galaxies, respectively, but now as a function of the clustercentric distance. For red galaxies, Fig. 16 shows that, beyond $\sim 0.4R_{200}$, galaxies show lower $\bar{n}$ values, for all filters, at farther distances from the cluster centre. For blue + green galaxies, Fig. 17 shows that $\bar{n}$ decreases, for all filters, up to $\sim 0.4R_{200}$, after that it remains constant with distance within the uncertainties. These results will be discussed in section 5.

4.4 Substructures in the Hydra Cluster and the phase-space diagram

The environment in which a galaxy is embedded may play an important role in determining its morphological (e.g. the n) and physical (e.g. the sSFR) parameters. The presence of substructures in a cluster can influence the parameters mentioned above. To check if this is the case in Hydra, we need to determine whether there are possible substructures within the cluster. The substructures generally have galaxies of different brightness, thus if we only use galaxies brighter than 16 (r-band) to check for the presence of substructure,
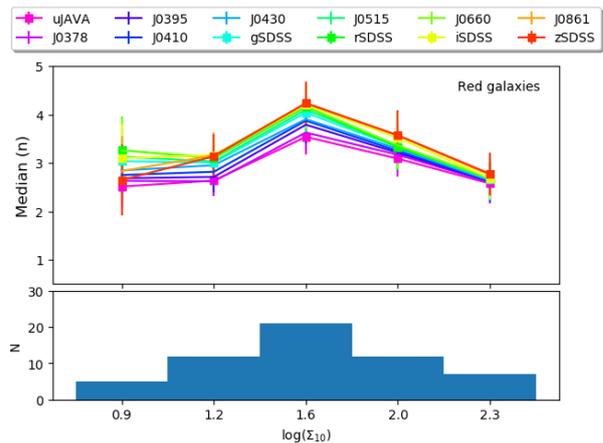
Figure 14. Sérsic index - Density relation for red galaxies. The top panel shows the $\bar{n}$, for each S-PLUS filter, with respect to the cluster density. The bottom panel shows a histogram with the number of galaxies per density bin.
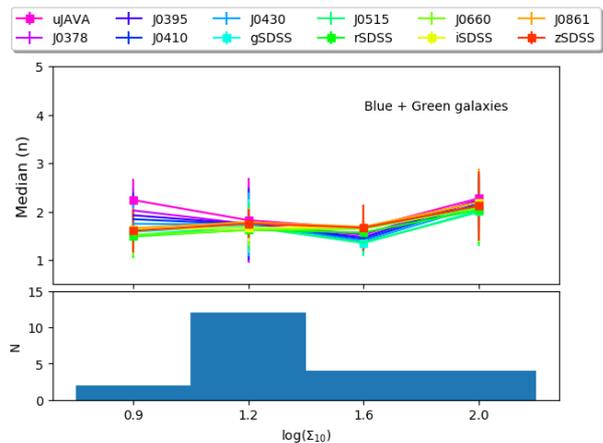

Figure 15. Same as Fig. 14, but for the blue + green galaxies.

we could lose important information. Therefore, we decide to use in this section the galaxies selected in Section 2.1, i.e. all the galaxies that have peculiar velocities lower than the escape velocity of the cluster, without considering any cut in magnitudes. There is a total of 193 such galaxies in Hydra and we apply the Dressler-Schectman test (DST, Dressler & Shectman 1988) on those galaxies to search for the existence of possible substructures. The DST estimates a Δ statistic for the cluster by comparing the kinematics of neighbouring galaxies with respect to the kinematics of the cluster. This comparison is done for each galaxy taking into account the N_{nn} nearest neighbours, where we use $N_{nn} = \sqrt{(N_{\text{total}})}$ following Pinkney et al. (1996), with N_{total} being the total
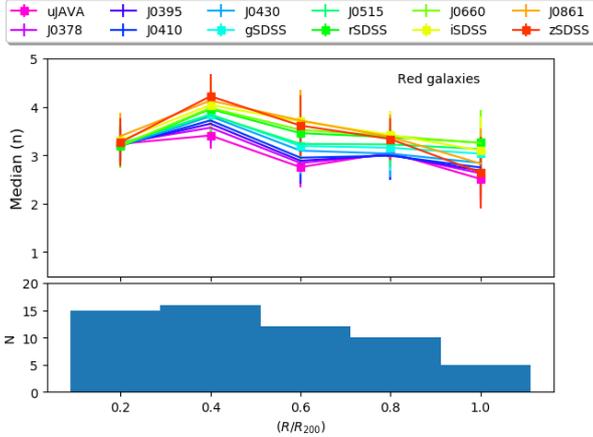
Figure 16. Sérsic index - Radius relation for red galaxies. The top panel shows the $\bar{n}$, for each S-PLUS filter, with respect to the cluster density. The bottom panel shows a histogram with the number of galaxies per (R/R_{200}) bin.
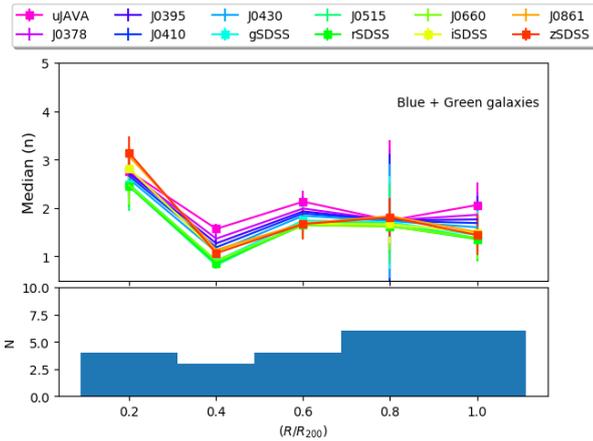

Figure 17. Same as Fig. 16, here for the blue + green galaxies.

number of objects in the Hydra cluster. Each galaxy and their N_{nn} neighbours are used to estimate a local mean velocity $\bar{v}_{local}$ and a local velocity dispersion σ_{local}, which are compared with the mean velocity $(\bar{v})$ and velocity dispersion (σ) of the cluster. For each galaxy we then estimate the iation δ as:

$$\delta^2 = (N_{nn}/\sigma^2)[(\bar{v}_{local} - \bar{v})^2 + (\sigma_{local} - \sigma^2)] \tag{17}$$

The Δ statistic is then defined as the cumulative deviation; $\Delta = \sum_i^N \delta_i$. If $\Delta/N_{\text{total}} > 1$ it means that probably there is a substructure in the cluster (White et al. 2015). For the Hydra cluster considering an area of $\sim 95'$ of radius and with 193 members, we found a $\Delta/N_{\text{total}} = 1.25$. To confirm that this result is significantly different from a random distribution, and validate the possible existence of substructures in Hydra, we calibrate the Δ statistic by randomly shuffling the velocities using a Monte Carlo simulation. We perform 1×10^5 iterations; for each of those we calculated the Δ statistic, which we call for simplicity random Δ. We then count the number of configurations for which the random
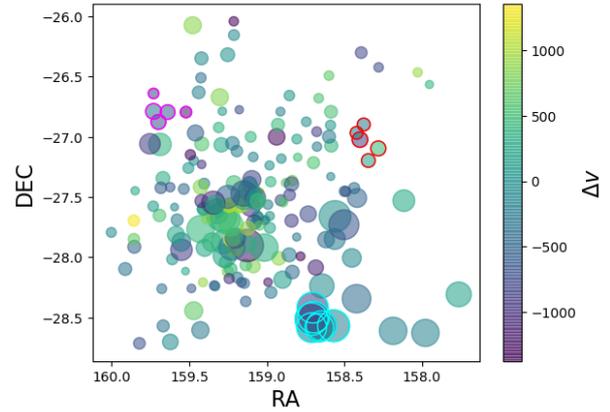
Figure 18. Spatial distribution of Hydra galaxies. The size of each circle is proportional to e^{δ}, i.e. bigger dots indicate that the galaxy is in a possible substructure. The galaxies are colour-coded by their peculiar velocity. The galaxies that belong to the different structures identified by DBSCAN are enclosed by open circles of different colours.

Δ is greater than the original Δ, N(Δ,randoms $> \Delta$), normalised by the number of iterations N(Δ,randoms), that is

$$P = \frac{N(\Delta, \text{randoms} > \Delta)}{N(\Delta, \text{randoms})} \tag{18}$$

If the fraction P is lower than 0.1, we can conclude that the original Δ value is not obtained from a random distribution (White et al. 2015). We find P = 0.016, which confirms a possible presence of substructures in the Hydra cluster.

In Fig. 18 we highlight the possible substructures detected in Hydra, where we show the distribution of the cluster's galaxies where the size of each circle is proportional to e^{δ}. Larger circles indicate a higher probability for a galaxy be part of a substructure. Each galaxy is colour-coded by their peculiar velocities with respect to the cluster's redshift. We found possible substructures in the outer regions of the cluster as well as in the central part, these possible substructures are enclosed by a black open square in Fig 20.

We note that Stein (1997) found that Hydra does not present any substructure, by applying the same DST but in an area of $45'$ radius (i.e half the area we use here), which includes 76 galaxies[2]. To understand this discrepancy we applied the DST in the same area as Stein (1997) using 136 galaxies, and found $\Delta/N_{\text{total}} = 1.0$, which is inconclusive in terms of substructures. Therefore, we detect possible new substructures in an unexplored area of Hydra.

In order to further look into the possibility of substructures, we use a Density-Based Spatial Clustering (DBSCAN, Ester et al. 1996) algorithm. DBSCAN takes as input the positions of the objects and the minimum number of objects with a maximum distance between them to be considered as a group/substructure. We adopt a maximum distance of 140 kpc and a minimum of 3 galaxies to consider a substructure (Sohn et al. 2015; Olave-Rojas et al. 2018). Using the 193

---

[2] We also note that, using the normality-test Stein (1997) found that Hydra presents substructures with 1 percent of significance level, see Beers et al. (1990b) for more details.
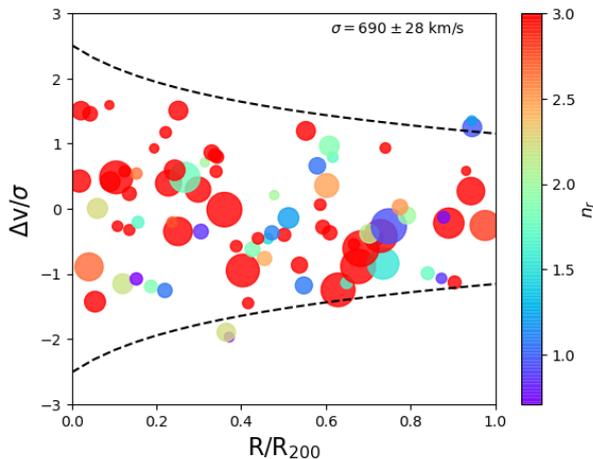
Figure 19. The phase-space diagram. The x-axis shows the projected distance from the cluster centre normalised by R_{200}. The y-axis shows the peculiar line-of-sight velocity with respect to the cluster recessional velocity, normalised by the velocity dispersion of the cluster. The dashed lines are the escape velocity defined in Jaffé et al. (2015, see their Eq. 2). Each galaxy is colour-coded by n_r. The colour bar saturates at n_r=3, thus all galaxies that have $n_r \geq 2.5$ are in red. The size of each circle is proportional to the δ of the DST.

Figure 20. Same as Fig. 19, colour-coded by $\log(sSFR)$. The grey dots are galaxies that do not have $H\alpha$ emission. Galaxies with $\delta >$ 3 times the standard deviation of δ distribution are enclosed by open black square.

5 DISCUSSION

We discuss in this section the results that we found in this work, interpret and compare them with previous studies. Also, we discuss few caveats and cautions that should be taken into account when interpreting some of the results presented here.

We find that $\bar{n}$ for ETGs, as well as red galaxies, displays a slight increase towards redder filters (13 percent of its value for red galaxies and 18 percent for ETGs, see Fig. 13). This result is in agreement with previous studies (La Barbera et al. 2010; Kelvin et al. 2012; Vulcani et al. 2014). For LTGs, we find that $\bar{n}$ decreases, from filter u to z, by 7 percent. However, other studies both in cluster and in field galaxies have found that n increases as a function of wavelength for LTGs (La Barbera et al. 2010; Kelvin et al. 2012; Vulcani et al. 2014; Psychogyios et al. 2019). This behaviour may be due to higher star formation in these galaxies, which is more concentrated in the inner regions. To better compare with Vulcani et al. (2014, hereafter V14) we have included their data points in Fig. 13. V14 used the filters u, g, r, i, and z from *SDSS*, and modelled field galaxies with a single Sérsic profile. We note, first, that their sample contains field galaxies and, second, that their colour cuts to separate galaxies as red, blue and green are slightly different than the one used in this work. Nevertheless, the green+blue and LTGs, from Hydra, show similar values of $\bar{n}$, within the uncertainties, with respect to the green galaxies in V14 for most filters. The $\bar{n}$ value for the u filter is higher for Hydra. For the red galaxies and filters u, g, and r our work and that of V14 show similar values of $\bar{n}$. However, galaxies in Hydra show a higher value in the filters i and z when compared to the field galaxies in V14. Overall galaxies in Hydra exhibit a higher value of $\bar{n}$ when compared to the blue galaxies of V14. This result is interesting and in agreement with Psychogyios et al. (2019), who found that cluster galaxies always have a higher value of $\bar{n}$, regardless of the filter, when compared to field galaxies. Thus, bearing in mind that a comparison with other studies is not so simple, due to the differences in separating galaxies as ETGs, LTGs, red, green and blue, which likely contribute to differences in the results, there may be

galaxies, `DBSCAN` finds the presence of three substructures within R_{200}, one of them in agreement with the possibility of a substructure found with the DST. Each galaxy that belongs to the substructure found by `DBSCAN` is enclosed by open circles in Fig 18. The galaxies that belong to the same structure found by DST are enclosed by cyan open circles; this substructure has 7 galaxies, 2 of them are SFGs.

Having determined the possible existence of substructures in Hydra, the phase-space diagram (Jaffé et al. 2015), which relates the distance to the cluster centre with the kinematical quantity $\Delta v/\sigma$, could help us to understand the dynamic state of Hydra. We show the phase-space diagram of Hydra in Fig. 19, where we use the 81 galaxies that have $m_r < 16$. The x-axis is the projected distance from the cluster centre normalised by R_{200} and the y-axis is the peculiar line-of-sight velocity of each galaxy with respect to the cluster recessional velocity, normalised by the velocity dispersion of the cluster. The escape velocity is indicated by the dashed lines and it is obtained based on a Navarro, Frenk & White dark matter profile (Navarro et al. 1996), see Jaffé et al. (2015) for more details. Figs. 19 and 20 show the same diagram colour-coded by n_r and $\log(sSFR)$, respectively, where the circle sizes are proportional to δ. We can see that there are galaxies both with higher and low n_r in possible substructures (bigger circles). Also, it is clear that some galaxies located in substructures are star forming. We can see from Fig. 20 that galaxies with larger δ are located beyond $0.6R_{200}$, and also some galaxies are closer to the cluster central region. Galaxies with $\delta \geq 3\sigma_\delta$ (the standard deviation of δ distribution) have the largest probability to belonging to a substructure (Girardi et al. 1997; Olave-Rojas et al. 2018). Fig 20 shows, enclosed by a black open square, the 12 galaxies that have $\delta \geq 3\sigma_\delta$. Four of these galaxies are near to the cluster centre and 8 are beyond $0.6R_{200}$. Two of the 12 galaxies are SFGs and 8 have $n_r \geq 2.5$.

actual differences between the $\bar{n}$ values as a function of filter between cluster and field galaxies. We will explore this further in a future work.

The $\bar{n}$ value for blue + green galaxies remains constant as a function of wavelength. We find that it appears to have a higher value for the bluest filters with respect to the clustercentric distance (Fig. 17). However, considering the uncertainties, we find no significant change in $\bar{n}$ as a function of distance or wavelength. We can see the same behaviour with respect to the density ($\log(\Sigma_{10})$), where $\bar{n}$ remains constant, considering the uncertainties (Fig. 15). The $\bar{n}$ for red galaxies is always greater than 2.5, and for blue + green galaxies is generally lower than 2. A similar result was presented in Psychogyios et al. (2019) using 5 filters (u, B, V, J and K). They found that the Sérsic index remains nearly constant as a function of wavelength, for galaxies that belong to a cluster.

Examining the Hydra's SMF we find that the ETGs and NSFGs are more massive and dominate the higher mass end of the global SMF (see Fig. 6), as expected for a cluster. The lower mass galaxies are mostly LTGs and SFGs and dominate the lower mass end of the SMF. These results are in agreement with previous studies (e.g., Blanton & Moustakas 2009; Vulcani et al. 2011; Etherington et al. 2017; van der Burg et al. 2020). For example, Vulcani et al. (2011) analysed a sample of 21 nearby clusters (0.04<z<0.07), finding that the global SMF is dominated by ETGs (Elliptical and S0 galaxies), while the number of late-type galaxies declines towards the high mass end of the SMF. In the local universe, the high mass end of the SMF is dominated by ETGs both in low and high-dense environments (Blanton & Moustakas 2009; Bell et al. 2003). The low mass end of the SMF for low-density environments is completely dominated by blue disk galaxies, whereas in high-dense environments there is a mix of ETGs and LTGs (Blanton & Moustakas 2009). Regarding the red galaxies, with the increase of local density (isolated − poor group − rich group − cluster), the characteristic mass of this population increases. This is because most of the brightest objects are red and located in dense regions. In addition, the blue population declines in importance as the local density increases (Blanton & Moustakas 2009).

In this work we separate galaxies as blue + green ($(u-r)$ < 2.3) and red ($(u-r) \geq 2.3$). There is an intermediate zone between the red sequence and the blue cloud, called green valley. These galaxies have typical colours between $1.8 < (u-r) < 2.3$ (Schawinski et al. 2014). In Hydra, we find that galaxies with colours $1.8 < (u-r) < 2.3$ do not present Hα emission. These objects could be transitional galaxies that have lower sSFRs than actively star-forming galaxies of the same mass. The galaxies in the green valley have very low levels of ongoing star formation (log (sSFR) < -10.8, Salim 2014), and we are not detecting star formation at such a low level. These galaxies do not meet the criteria required to be considered as emission line galaxies, i.e. to have a genuine narrow-band colour excess (the 3Σ cut and the have $EW_{J0660} > 12$ Å). It is possible that these objects have Hα emission below the detection limit of the survey. Perhaps, in some of these galaxies, deeper images will evidence Hα emission. Most of these objects appear located in the outskirts of the cluster, which suggests that these have fallen into the cluster recently; however these have already suffered the in-

fluence of the cluster, and may already have lost some or a considerable amount of their gas, which might be another possibility to explain the absence of Hα emission. We therefore suggest that this population of green galaxies could have stopped their star formation recently due to environmental effects (Peng et al. 2010b; Wright et al. 2019).

As it is well known, the morphology and SFR of galaxies are correlated, and the environment likely plays an important role in the evolutionary changes of these parameters (Paulino-Afonso et al. 2019; Pallero et al. 2019; Fasano et al. 2015). In this work we study the behaviour of sSFR with respect to the clustercentric distance and density. We find that ~ 88 percent of the Hydra' galaxies are quenched, based on their Hα emission. However, 23 percent of Hydra galaxies are LTGs, according to our morphological and physical classification. This suggests that, as advocated by Liu et al. (2019), the galactic physical properties (e.g. SFR) of galaxies in a cluster change faster than their structural properties.

The Dressler-Schectman test we performed in the previous section indicates that Hydra presents substructures with a $\Delta/N_{\text{total}} = 1.25$. This value is not too high in comparison with other clusters (see as a example Olave-Rojas et al. 2018). We also confirm the presence of substructures using the DBSCAN algorithm. Interestingly, previous studies have shown that Hydra has an approximately homogeneous X-ray distribution. This observed feature suggests that the cluster has not suffered merging processes recently, and probably is a relaxed system (Fitchett & Merritt 1988; Furusho et al. 2001; Hayakawa et al. 2004; Łokas et al. 2006). It was also found in other work that Hydra does not present a Gaussian velocity distribution (Fitchett & Merritt 1988). Combining the previous information with our findings of substructures in Hydra, we conclude that Hydra is disturbed/perturbed, but not significantly and thus it is very close to become a virialized system.

S-PLUS will observe a huge area around Hydra Cluster, which we will use to study the behaviour of the galaxies in a less dense environment, but still under the influence of the cluster (beyond $1R_{200}$). In a upcoming work, we will also study the morphological and physical parameters of the bulge and the disc components of Hydra galaxies, separately. In the case of the substructures in the Hydra cluster, deeper images will allow us to see if the substructures can be correlated to intracluster light. In addition, these observations will be compared with state-of-the-art hydrodynamical simulations such as IllUSTRIS-TNG (Nelson et al. 2018) and C-EAGLE (Barnes et al. 2018) in order to understand the evolutionary processes responsible of the observed properties of the Hydra cluster galaxies.

6   SUMMARY AND CONCLUSIONS

This is the first of a series of papers exploring the evolution of galaxies in dense environments. We used the Hydra Cluster as a laboratory to study galaxy evolution, more specifically to explore the structural and physical properties of galaxies with respect to the environment. The analysis done in this work is based on S-PLUS data, a survey that has 12 filters in the visible range of the spectrum and a camera with a field of view of ~ 2 square degree. The area studied here

involves four S-PLUS fields, covering approximately a region of 1.4 Mpc radius centered on the Hydra cluster. We analyse the derived structural and physical parameters of a selected sample of 81 Hydra galaxies. All of them are brighter than 16 mag (r-band) and are part of the cluster.

Our main findings are:

1) There is a clear correlation between n_r and the galaxy stellar mass. Higher values of n_r are found for larger stellar masses. The sSFR has the opposite behaviour, the higher the n_r, the lower is the sSFR, as expected (see Figures 8 and 9).

2) There is a larger fraction of NSFGs (galaxies with $\log(sSFR) \leq$ -11), than SFGs (galaxies with $\log(sSFR) >$ -11) across all R_{200} and all cluster densities. We find that $\sim$88 percent of Hydra galaxies can be classified as NSFG.

3) The $\bar{n}$ changes with the colour of the galaxies. The $\bar{n}$ for red and ETGs present an increase of 13 and 18 percent respectively, towards redder wavelengths. The LTGs shows a decrease in $\bar{n}$ (7 percent), from u to z band, while the $\bar{n}$ for blue + green galaxies remains constant. Beyond $\sim$0.3R$_{200}$ red galaxies show lower $\bar{n}$ values, for all filters, declining as a function of distance from the cluster centre. The $\bar{n}$ for blue + green galaxies remains constant for all filters.

4) We find that the Hydra cluster presents possible substructures, as determined from a Dressler-Schectman test (DST). The Density-Based Spatial Clustering `DBSCAN` algorithm found a substructure with exactly the same galaxies as one of the substructures detected by the DST. Two of the galaxies that are in that likely substructure are SFG, and lie in front of the cluster centre, based on the phase-space diagram. We speculate that these galaxies are falling now in to the cluster. However, given that there are few substructure, we conclude that the Hydra cluster is, although perturbed, close to virialization.

DATA AVAILABILITY

The data used in this article is from an internal release of the S-PLUS. This means that the sample studied here is not publicly available now but will be included in the next public data release of S-PLUS.

REFERENCES

Abadi M. G., Moore B., Bower R. G., 1999, MNRAS, 308, 947
Abazajian K. N., et al., 2009, ApJS, 182, 543
Arnaboldi M., Ventimiglia G., Iodice E., Gerhard O., Coccato L., 2012, A&A, 545, A37
Arnouts S., Cristiani S., Moscardini L., Matarrese S., Lucchin F., Fontana A., Giallongo E., 1999, MNRAS, 310, 540
Babyk I. V., Vavilova I. B., 2013, Odessa Astronomical Publications, 26, 175
Balogh M. L., Morris S. L., 2000, MNRAS, 318, 703
Bamford S. P., Häußler B., Rojas A., Borch A., 2011, in Evans I. N., Accomazzi A., Mink D. J., Rots A. H., eds, Astronomical Society of the Pacific Conference Series Vol. 442, Astronomical Data Analysis Software and Systems XX. p. 479
Barbosa C. E., Arnaboldi M., Coccato L., Gerhard O., Mendes de Oliveira C., Hilker M., Richtler T., 2018, A&A, 609, A78
Barnes L. A., et al., 2018, MNRAS, 477, 3727
Bautz L. P., Morgan W. W., 1970, ApJ, 162, L149
Beers T. C., Flynn K., Gebhardt K., 1990a, AJ, 100, 32
Beers T. C., Flynn K., Gebhardt K., 1990b, AJ, 100, 32
Bell E. F., McIntosh D. H., Katz N., Weinberg M. D., 2003, ApJS, 149, 289
Bell E. F., et al., 2004, ApJ, 608, 752
Bertin E., Arnouts S., 1996, A&AS, 117, 393
Blanton M. R., Moustakas J., 2009, ARA&A, 47, 159
Boselli A., et al., 2005, ApJ, 629, L29
Bruzual G., Charlot S., 2003, MNRAS, 344, 1000
Bruzual A. G., Charlot S., 1993, ApJ, 405, 538
Butcher H., Oemler A. J., 1978, ApJ, 226, 559
Calzetti D., Armus L., Bohlin R. C., Kinney A. L., Koornneef J., Storchi-Bergmann T., 2000, ApJ, 533, 682
Cantalupo S., 2010, MNRAS, 403, L16
Cardelli J. A., Clayton G. C., Mathis J. S., 1989, ApJ, 345, 245
Cenarro A. J., et al., 2019, A&A, 622, A176
Chabrier G., 2003, PASP, 115, 763
Cicone C., et al., 2014, A&A, 562, A21
Cid Fernandes R., Mateus A., Sodré L., Stasińska G., Gomes J. M., 2005, MNRAS, 358, 363
Coe D., et al., 2012, ApJ, 757, 22
Comerford J. M., Natarajan P., 2007, MNRAS, 379, 190
Cora S. A., Hough T., Vega-Martínez C. A., Orsi A. A., 2019, Boletin de la Asociacion Argentina de Astronomia La Plata Argentina, 61, 204
Croton D. J., et al., 2006, MNRAS, 365, 11
Davis M., Geller M. J., 1976, ApJ, 208, 13
Dekel A., Silk J., 1986, ApJ, 303, 39
Desai V., et al., 2007, ApJ, 660, 1151
Diaferio A., 1999, MNRAS, 309, 610

Dimauro P., et al., 2018, MNRAS, 478, 5410
Dobrycheva D. V., Vavilova I. B., Melnyk O. V., Elyiv A. A., 2017, preprint, (arXiv:1712.08955)
Dressler A., 1980, ApJ, 236, 351
Dressler A., Shectman S. A., 1988, AJ, 95, 985
Dressler A., et al., 1997, ApJ, 490, 577
Duc P.-A., Bournaud F., 2008, ApJ, 673, 787
Efstathiou G., 2000, MNRAS, 317, 697
Ester M., Kriegel H.-P., Sander J., Xu X., 1996, in Proceedings of the Second International Conference on Knowledge Discovery and Data Mining. KDD'96. AAAI Press, pp 226–231, http://dl.acm.org/citation.cfm?id=3001460.3001507
Etherington J., et al., 2017, MNRAS, 466, 228
Faber S. M., Gallagher J. S., 1979, ARA&A, 17, 135
Fabian A. C., 2012, ARA&A, 50, 455
Fasano G., Poggianti B. M., Couch W. J., Bettoni D., Kjærgaard P., Moles M., 2000, ApJ, 542, 673
Fasano G., et al., 2015, MNRAS, 449, 3927
Fitchett M., Merritt D., 1988, ApJ, 335, 18
Furusho T., et al., 2001, PASJ, 53, 421
Gil de Paz A., et al., 2007, ApJS, 173, 185
Girardi M., Escalera E., Fadda D., Giuricin G., Mardirossian F., Mezzetti M., 1997, ApJ, 482, 41
Gonzalez E. J., et al., 2018, A&A, 611, A78
Gunn J. E., Gott J. Richard I., 1972, ApJ, 176, 1
Harrison E. R., 1974, ApJ, 191, L51
Hatfield P. W., Jarvis M. J., 2017, MNRAS, 472, 3570
Häußler B., et al., 2013, MNRAS, 430, 330
Hayakawa A., Furusho T., Yamasaki N. Y., Ishida M., Ohashi T., 2004, PASJ, 56, 743
Hopkins A. M., Connolly A. J., Haarsma D. B., Cram L. E., 2001, AJ, 122, 288
Ilbert O., et al., 2006, A&A, 457, 841
Jaffé Y. L., Smith R., Candlish G. N., Poggianti B. M., Sheen Y.-K., Verheijen M. A. W., 2015, MNRAS, 448, 1715
Jones D. H., et al., 2004, MNRAS, 355, 747
Kartaltepe J. S., et al., 2015, ApJS, 221, 11
Kelvin L. S., et al., 2012, MNRAS, 421, 1007
Kennedy R., et al., 2015, MNRAS, 454, 806
Kennicutt Robert C. J., 1992, ApJ, 388, 310
Kennicutt Jr. R. C., 1998, ApJ, 498, 541
Khostovan A. A., et al., 2020, MNRAS, 493, 3966
Koyama Y., et al., 2013, MNRAS, 434, 423
La Barbera F., de Carvalho R. R., de La Rosa I. G., Lopes P. A. A., Kohl-Moreira J. L., Capelato H. V., 2010, MNRAS, 408, 1313
Laganá T. F., Ulmer M. P., 2018, MNRAS, 475, 523
Larson R. B., 1974, MNRAS, 169, 229
Lauer T. R., et al., 1995, AJ, 110, 2622
Lee J. H., Lee M. G., Kim T., Hwang H. S., Park C., Choi Y.-Y., 2007, ApJ, 663, L69
Leonard A., King L. J., 2010, Monthly Notices of the Royal Astronomical Society, 405, 1854
Lintott C. J., et al., 2008, MNRAS, 389, 1179
Liu S.-F., et al., 2011, AJ, 141, 99
Liu C., Hao L., Wang H., Yang X., 2019, ApJ, 878, 69
Łokas E. L., Wojtak R., Gottlöber S., Mamon G. A., Prada F., 2006, MNRAS, 367, 1463
Lotz J. M., Primack J., Madau P., 2004, AJ, 128, 163
Lotz J. M., et al., 2008, ApJ, 672, 177
Ly C., et al., 2007, ApJ, 657, 738
Ly C., Malkan M. A., Kashikawa N., Ota K., Shimasaku K., Iye M., Currie T., 2012, ApJ, 747, L16
Mendes de Oliveira C., et al., 2019, MNRAS, p. 2048
Misgeld I., Hilker M., 2011, MNRAS, 414, 3699
Misgeld I., Mieske S., Hilker M., Richtler T., Georgiev I. Y., Schuberth Y., 2011, A&A, 531, A4
Moffat A. F. J., 1969, A&A, 3, 455
Molino A., et al., 2019, arXiv e-prints, p. arXiv:1907.06315
Moore B., Lake G., Katz N., 1998, ApJ, 495, 139
Moore B., Lake G., Quinn T., Stadel J., 1999, MNRAS, 304, 465
Munari E., Biviano A., Borgani S., Murante G., Fabjan D., 2013, MNRAS, 430, 2638
Navarro J. F., Frenk C. S., White S. D. M., 1996, ApJ, 462, 563
Nelson D., et al., 2018, MNRAS, 475, 624
Oemler Augustus J., 1974, ApJ, 194, 1
Olave-Rojas D., Cerulo P., Demarco R., Jaffé Y. L., Mercurio A., Rosati P., Balestra I., Nonino M., 2018, MNRAS, 479, 2328
Owers M. S., et al., 2019, ApJ, 873, 52
Pallero D., Gómez F. A., Padilla N. D., Torres-Flores S., Demarco R., Cerulo P., Olave-Rojas D., 2019, MNRAS, 488, 847
Papovich C., Dickinson M., Giavalisco M., Conselice C. J., Ferguson H. C., 2005, ApJ, 631, 101
Park C., Choi Y.-Y., 2005, ApJ, 635, L29
Pascual S., Gallego J., Zamorano J., 2007, PASP, 119, 30
Paulino-Afonso A., et al., 2019, A&A, 630, A57
Peng C. Y., Ho L. C., Impey C. D., Rix H.-W., 2002, AJ, 124, 266
Peng C. Y., Ho L. C., Impey C. D., Rix H.-W., 2010a, AJ, 139, 2097
Peng Y.-j., et al., 2010b, ApJ, 721, 193
Peng Y., Maiolino R., Cochrane R., 2015, Nature, 521, 192
Pinkney J., Roettiger K., Burns J. O., Bird C. M., 1996, ApJS, 104, 1
Poggianti B. M., et al., 2001, ApJ, 562, 689
Postman M., Geller M. J., 1984, ApJ, 281, 95
Postman M., et al., 2005, ApJ, 623, 721
Psychogyios A., et al., 2019, arXiv e-prints, p. arXiv:1909.03256
Quilis V., Moore B., Bower R., 2000, Science, 288, 1617
Richter O. G., 1987, A&AS, 67, 237
Rodríguez-Muñoz L., et al., 2019, MNRAS, 485, 586
Ruel J., et al., 2014, ApJ, 792, 45
Salim S., 2014, Serbian Astronomical Journal, 189, 1
Salpeter E. E., 1955, ApJ, 121, 161
Schawinski K., et al., 2014, MNRAS, 440, 889
Schlegel D. J., Finkbeiner D. P., Davis M., 1998, ApJ, 500, 525
Sérsic J. L., 1963, Boletin de la Asociacion Argentina de Astronomia La Plata Argentina, 6, 41
Simmons B. D., et al., 2017, MNRAS, 464, 4420
Skrutskie M. F., et al., 1997, The Two Micron All Sky Survey (2MASS): Overview and Status.. p. 25, doi:10.1007/978-94-011-5784-1_4
Smith R., et al., 2015, MNRAS, 454, 2502
Sobral D., Best P. N., Matsuda Y., Smail I., Geach J. E., Cirasuolo M., 2012, MNRAS, 420, 1926
Sohn J., Hwang H. S., Geller M. J., Diaferio A., Rines K. J., Lee M. G., Lee G.-H., 2015, Journal of Korean Astronomical Society, 48, 381
Spergel D. N., et al., 2003, ApJS, 148, 175
Stein P., 1996, A&AS, 116, 203
Stein P., 1997, A&A, 317, 670
Taylor E. N., et al., 2011, MNRAS, 418, 1587
Ventimiglia G., Arnaboldi M., Gerhard O., 2011, A&A, 528, A24
Vika M., Bamford S. P., Häußler B., Rojas A. L., Borch A., Nichol R. C., 2013, MNRAS, 435, 623
Vika M., Bamford S. P., Häußler B., Rojas A. L., 2014, MNRAS, 444, 3603
Vika M., Vulcani B., Bamford S. P., Häußler B., Rojas A. L., 2015, A&A, 577, A97
Vilella-Rojo G., et al., 2015, A&A, 580, A47
Vollmer B., Cayatte V., Balkowski C., Duschl W. J., 2001, ApJ, 561, 708
Vulcani B., et al., 2011, MNRAS, 412, 246
Vulcani B., et al., 2014, ApJ, 797, 62
Weinmann S. M., Kauffmann G., von der Linden A., De Lucia G., 2010, MNRAS, 406, 2249

Wetzel A. R., Tinker J. L., Conroy C., 2012, MNRAS, 424, 232

Wetzel A. R., Tinker J. L., Conroy C., van den Bosch F. C., 2013, MNRAS, 432, 336

Wetzel A. R., Tinker J. L., Conroy C., van den Bosch F. C., 2014, MNRAS, 439, 2687

White J. A., et al., 2015, MNRAS, 453, 2718

Whitmore B. C., Gilmore D. M., 1991, ApJ, 367, 64

Wright E. L., et al., 2010, AJ, 140, 1868

Wright R. J., Lagos C. d. P., Davies L. J. M., Power C., Trayford J. W., Wong O. I., 2019, MNRAS, 487, 3740

Yan P.-F., Yuan Q.-R., Zhang L., Zhou X., 2014, AJ, 147, 106

da Cunha E., Charlot S., Dunne L., Smith D., Rowlands K., 2012, in Tuffs R. J., Popescu C. C., eds, IAU Symposium Vol. 284, The Spectral Energy Distribution of Galaxies - SED 2011. pp 292–296 (arXiv:1111.3961), doi:10.1017/S1743921312009283

van der Burg R. F. J., et al., 2020, A&A, 638, A112

APPENDIX A: DATA TABLES

In this Appendix we present an example of the tables with the photometric information of each galaxy as well as their parameters determined in this work. Details about how these parameters were determined are found in Sections 3.1, 3.2 and 3.3. Full versions of these tables can be downloaded from the online version of the paper.

APPENDIX B: SIMULATED GALAXIES

.

In order to prove the goodness of GALFITM on retrieving structural parameters and physical information, we generated a set of five simulated galaxies to be modelled by GALFITM. The simulated galaxies were generated in each of all SPLUS-filters, using the same range of observational parameters as in the observations (S/N, filters and background level). We use a star-forming SED (SF) and a quiescent SED (Q) to model a realistic wavelenght dependance of the flux. On this exercise, we fix the Sérsic index over all wavelength, letting free the total flux. GALFITM allows us to recover the Sérsic index and effective radius with an uncertainty $\sim$4 percent with respect to the value used in the construction of the simulated galaxy. In addition, we perform a linear regression, comparing the magnitudes of the simulated galaxies with respect to the magnitudes found by GALFITM. We find a coefficient of determination of $\sim$1. These results confirm that the parameters recovered by the GALFITM models are reliable. Table B1 lists the magnitudes in all 12 S-PLUS filters, n_r, $R_{e,r}$ and the SED used in the five simulated galaxies (Input simulation) and those recovered by GALFITM (GALFITM output). Figures B1, B2, B3, B4 and B5, show the 5 modelled galaxies. On these figures, top panels show the simulated galaxies, middle panels show the GALFITM models and bottom panels show the residuals, derived from the subtraction between the top and middle panels.

This paper has been typeset from a TEX/LATEX file prepared by the author.

Table A1. Magnitudes estimated in this work using MegaMorph project. Column 1 is the ID of each galaxy, and the columns 2 to 13 are the magnitudes in the 12 S-PLUS filters, without the correction for Galactic extinction. A full version of this table, for all galaxies, is available as supporting information in the online version of this manuscript.

ID	u	J0378	J0395	J0410	J0430	g	J0515	r	J0660	i	J0861	z
1	15.41±0.01	15.05±0.02	14.81±0.02	14.62±0.01	14.43±0.01	14.12±0.01	13.91±0.1	13.45±0.1	13.19±0.01	13.09±0.01	12.93±0.02	12.87±0.01

Table A2. Sérsic index estimated in this work using MegaMorph project. Column 1 is the ID of each galaxy, and the columns 2 to 13 are the Sérsic index in the 12 S-PLUS filters. A full version of this table, for all galaxies, is available as supporting information in the online version available as supporting information in the online version.

ID	u	J0378	J0395	J0410	J0430	g	J0515	r	J0660	i	J0861	z
1	1.36±0.02	1.23±0.02	1.17±0.02	1.12±0.01	1.07±0.01	0.97±0.02	0.94±0.01	0.95±0.01	0.99±0.01	1.10 ±0.01	1.15 ±0.01	1.13 ±0.01

Table A3. Physical parameters of the galaxies. Column 1 is the ID of each galaxy, columns 2 and 3 are the right ascension and declination respectively. The stellar mass calculated with the colour $(g-i)$ presented in Taylor et al. (2011) is in column 4. The luminosity and sSFR are in the columns 5 and 6 respectively. A full version of this table, for all galaxies, is available as supporting information in the online version of this manuscript.

ID	RA° J2000	DEC° J2000	$\log(M_\star/M_\odot)$	$L_{H\alpha}$ $10^{39}\mathrm{ergs}^{-1}$	$\log(sSFR/yr)$
1	159.67	-28.57	10.01±0.05	64.48±7.34	-10.01±0.06

Table B1. Magnitudes for 5 simulated galaxies (Input Model) and its magnitudes recovered by GALFITM (GALFITM output)

Galaxy	u	J0378	J0395	J0410	J0430	g	J0515	r	J0660	i	J0861	z	n_r	$R_{e,r}$ (arcsec)	SED
1 Input simulation	13.75	13.53	13.34	13.08	12.59	12.17	11.90	11.52	11.45	11.20	11.04	11.00	2.00	10.00	Q
1 GALFITM output	13.74	13.52	13.33	13.07	12.58	12.16	11.89	11.50	11.44	11.19	11.03	11.00	1.98	10.02	
2 Input simulation	13.75	13.53	13.34	13.08	12.59	12.17	11.90	11.52	11.45	11.20	11.04	11.00	4.00	10.00	Q
2 GALFITM output	13.69	13.47	13.28	13.02	13.53	12.11	11.84	11.46	11.39	11.14	10.98	10.94	3.87	9.96	
3 Input simulation	14.41	14.30	14.11	13.57	13.28	13.20	13.14	13.08	13.08	13.04	13.01	13.00	4.00	20.00	SF
3 GALFITM output	14.34	14.24	14.05	13.50	13.21	13.13	13.08	13.02	13.02	12.98	12.94	12.93	3.85	19.65	
4 Input simulation	14.41	14.30	14.11	13.57	13.28	13.20	13.14	13.08	13.08	13.04	13.01	13.00	5.00	10.00	SF
4 GALFITM output	14.33	14.22	14.03	13.48	13.19	13.11	13.05	13.00	13.00	12.96	12.92	12.92	4.82	9.68	
5 Input simulation	14.41	14.30	14.11	13.57	13.28	13.20	13.14	13.08	13.08	13.04	13.01	13.00	1.00	20.00	SF
5 GALFITM output	14.42	14.31	14.11	13.56	13.27	13.19	13.13	13.08	13.07	13.04	13.00	12.99	0.99	20.01	
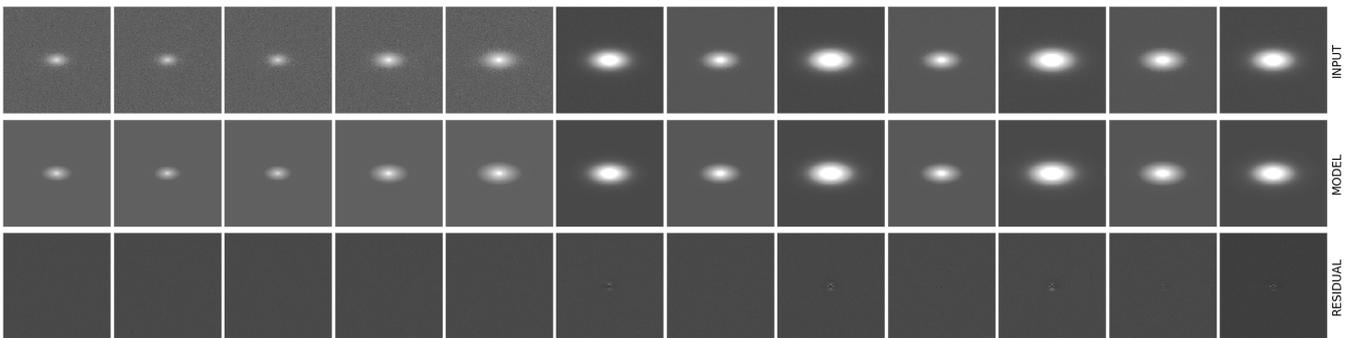
Figure B1. Simulated galaxy 1 (top panels), the GALFITM models (middle panels), and the residual image (observed minus modelled – bottom panels).
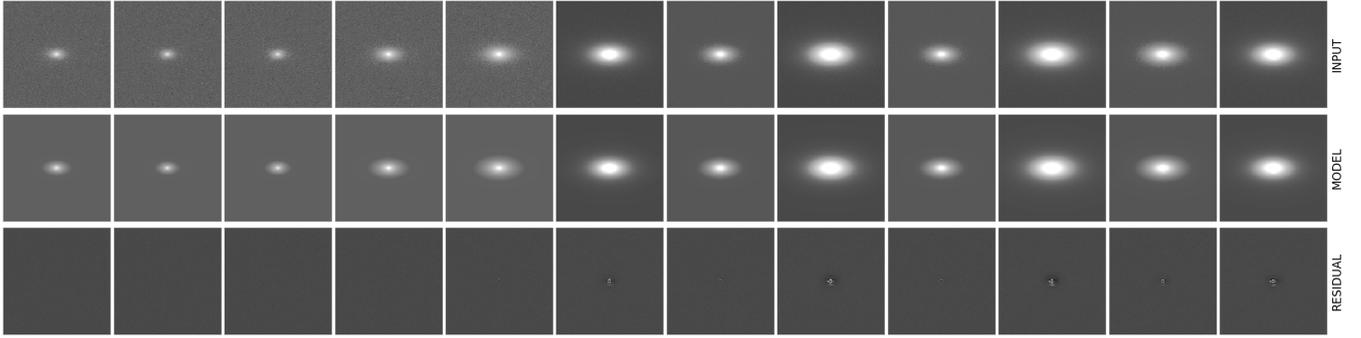
Figure B2. Simulated galaxy 2 (top panels), the GALFITM models (middle panels), and the residual image (observed minus modelled – bottom panels)
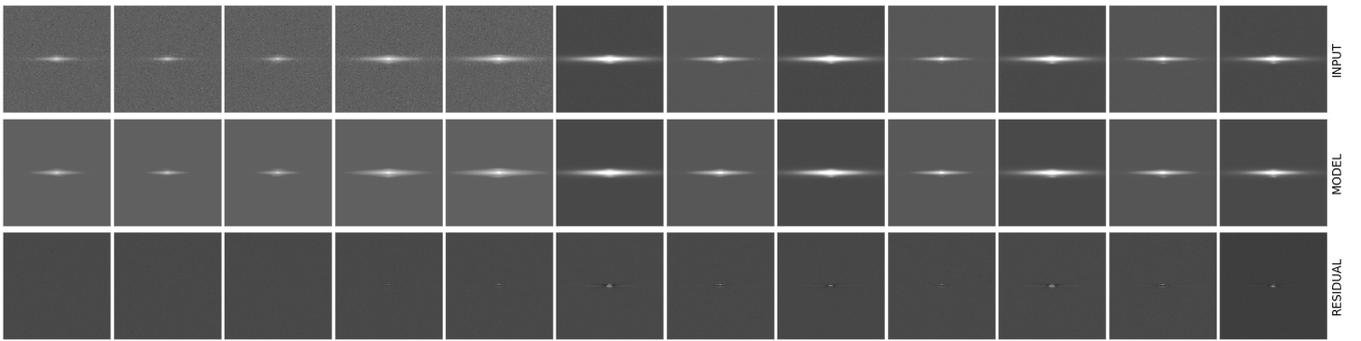

Figure B3. Simulated galaxy 3 (top panels), the GALFITM models (middle panels), and the residual image (observed minus modelled – bottom panels).
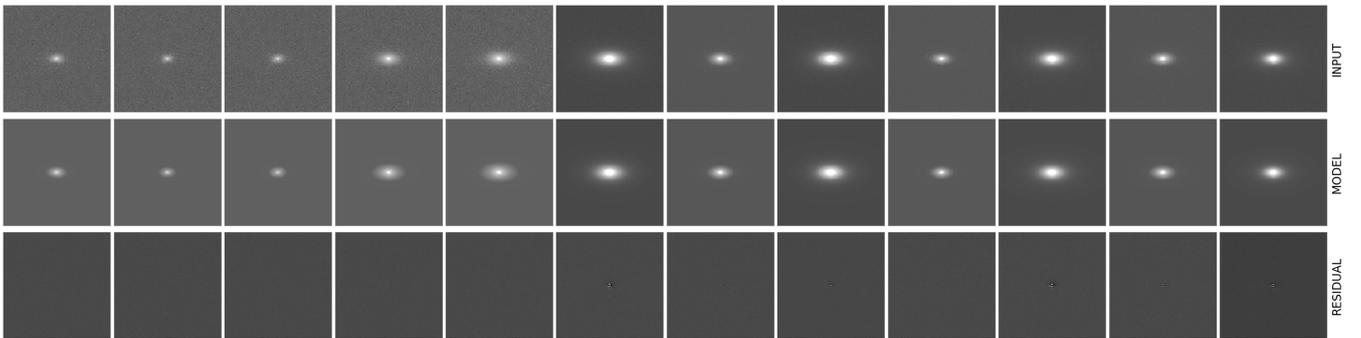

Figure B4. Simulated galaxy 4 (top panels), the GALFITM models (middle panels), and the residual image (observed minus modelled – bottom panels).
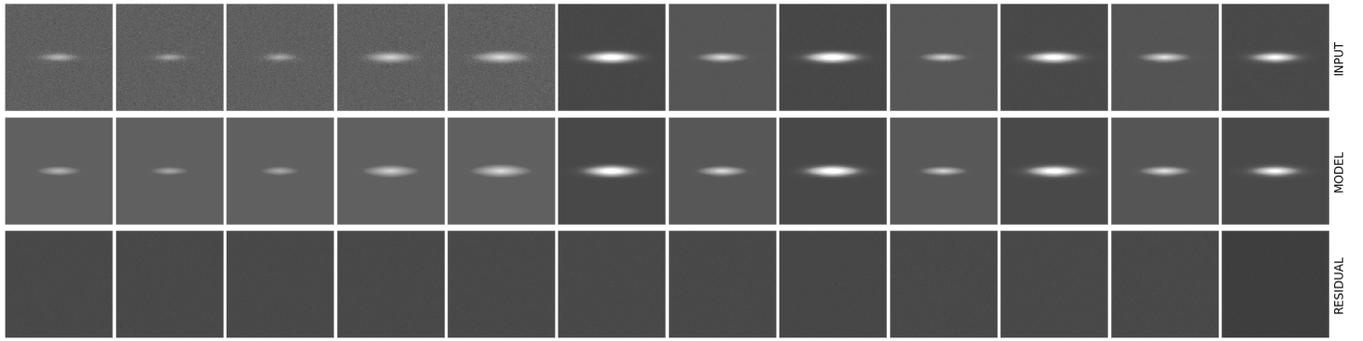
Figure B5. Simulated galaxy 5 (top panels), the GALFITM models (middle panels), and the residual image (observed minus modelled – bottom panels).